Journal of Sound and Vibration (2000) **230**(2), 411–446
doi:10.1006/jsvi.1999.2616, available online at http://www.idealibrary.com on IDEAL®

MODE STRUCTURE FOR FLUID–SOLID MEDIA AS DERIVED BY LOW-FREQUENCY ASYMPTOTICS

S. IVANSSON

Division of Systems and Underwater Technology, Defence Research Establishment, SE-172 90 Stockholm, Sweden

(*Received* 29 *March* 1999, *and in final form* 8 *September* 1999)

The modes in a laterally homogeneous fluid–solid medium can be classified according to their low-frequency behaviour. For each mode, the horizontal wavenumber $k(\omega)$ will tend to a complex limit q (possibly infinite, but that appears to be exceptional) as the angular frequency ω tends to zero. The modes with vanishing wavenumber limits q can be listed explicitly, they are finite in number for each particular medium. The non-zero finite limits q appear as the zeros of certain entire analytic functions, one particular function for each fluid or solid region in the medium (and also for each Riemann sheet in the presence of homogeneous half-spaces). The resulting low-frequency mode structure can be uncovered for each fluid–solid medium by computing the wavenumber limits q as provided by the different regions. Efficient and reliable numerical techniques for this purpose are proposed for homogeneously layered media, based on compound-matrix factorization. The mode structure can be carried to higher frequencies by tracking dispersion curves. The behaviour at double roots and branch points needs special consideration. Two examples are studied in detail, one from plate acoustics and one from underwater acoustics.

1. INTRODUCTION

The mode structure for a horizontally infinite, homogeneous and isotropic, fluid plate with free or rigid boundaries in depth is very simple [1, section 3.1]. It can be recovered directly from the dispersion function, a simple cosine or sine [2, section 5.4]. Without absorption, the horizontal wavenumber for each mode will move from the real to the imaginary axis as the frequency is decreased, with a double root at the origin for the cut-off frequency. As the frequency is further decreased towards zero, the modal wavenumber will tend to a non-vanishing imaginary constant q given by $\cosh(qd) = 0$ or $\sinh(qd) = 0$, where d is the thickness of the plate.

The mode structure for a corresponding solid plate is much more complicated, although the dispersion function can still be expressed explicitly in terms of elementary functions (the Rayleigh–Lamb dispersion function). Much progress was made by Mindlin and his associates, see references [3–5]. It became clear that the dispersion trajectories consist of purely real, purely imaginary, and complex branches. For a free plate, Sherwood [6] noted that the modal wavenumbers will

0022-460X/00/070411 + 36 $35.00/0

tend to complex limits q as the frequency tends to zero, where

$$\sinh(qd) \pm qd = 0 \tag{1}$$

with d denoting the thickness of the plate. Useful reviews of these and other results can be found in, e.g., references [7, section 6.8; 8]. Plates for which the Poisson ratio is negative have been considered rather recently by Freedman [9].

Media with fluid and solid regions combined have also attracted interest. Rokhlin *et al.* [10], Freedman [11], and Bao *et al.* [12], among others, have studied the effects of fluid loading on Lamb mode spectra for homogeneous solid plates. In this context, Crighton [13] has provided a useful discussion of the significance of leaky modes, with an unphysical exponential increase or inward direction of oscillation in the fluid half-space (s). Trilayers, with two homogeneous solid plates separated by fluid, have been considered in references [14, 15]. In all of these studies, homogeneous isotropic fluid and solid regions were assumed, and the dispersion function could be given explicitly in terms of elementary trigonometric or hyperbolic functions.

Fluid–solid media with an arbitrary number of fluid and solid regions, and with a general variation with depth for the velocity and density parameters, were considered by Ivansson [16, 17]. By an asymptotic study of the dispersion function, all normal modes for which the horizontal wavenumber tends to zero with the frequency could be determined explicitly. Normal modes with non-vanishing but finite low-frequency wavenumber limits were shown to fall into region-dependent classes, one class of modes for each fluid and each solid region in the medium.

It is the purpose of the present paper to further explore these recent results and their implications for the mode structure of fluid–solid media. Efficient and reliable techniques for computing the low-frequency wavenumber limits have to be developed. Tracking dispersion curves as the frequency is varied will be the essential tool for carrying the low-frequency mode structure to higher frequencies.

To be precise, the paper is concerned with laterally homogeneous, also called range-independent, fluid–solid media that are linearly viscoelastic (absorption is allowed) and isotropic. The medium properties are assumed to vary with z only, where z is the depth co-ordinate. By "fluid–solid" we mean that there are a finite number of regions is depth, each of fluid or solid type. The medium can be terminated above and below by traction-free, rigid, or (for a solid region) mixed-condition boundaries, or by homogeneous fluid or solid half-spaces. The mixed-condition boundary is characterized by vanishing horizontal displacement and normal traction. A homogeneous half-space is itself considered as (part of) a fluid or solid region. All regions will have non-vanishing thickness, with the exception that we will allow a medium with some solid region to be terminated by a fluid region with vanishing thickness and a rigid boundary. This is obviously equivalent to a particular type of boundary conditions at the adjacent solid region: vanishing vertical displacement and shear traction.

Only mono-frequency P-SV wave propagation, with harmonic time dependence $\mathrm{e}^{-\mathrm{i}\omega t}$ assumed throughout, where $\omega = 2\pi f > 0$ is the angular frequency and t is time, is considered. The complex horizontal slowness and the complex horizontal

wavenumber are denoted by p and $k = \omega p$, respectively. $D(\omega, p)$ is the dispersion function, whose zeros determine the modal p. In the presence of homogeneous half-spaces, more than one Riemann sheet appears and $D(\omega, p)$ is multi-valued.

The plan of the paper is as follows. Section 2 is devoted to a brief presentation of the essential results needed from references [16, 17]. A heuristic proof of a key result on asymptotic low-frequency medium separation is included. Section 3 is restricted to homogeneously layered media. It is shown how the dispersion function $D(\omega, p)$ can be computed very efficiently by compound-matrix factorization. Some problems concerning mode tracking are addressed in section 4: passage of double roots and branch points. A numerical cancellation problem is dealt with in Appendix A. The mode structure is determined and analyzed in detail for two particular media in sections 5 and 6. These examples concern plate acoustics (section 5) and underwater acoustics (section 6). The final section 7 contains some conclusions and some problems for further research.

2. LOW-FREQUENCY MODE STRUCTURE ACCORDING TO REFERENCES [16, 17]

The Lamé parameters for a fixed frequency are denoted by $\lambda(z)$ and $\mu(z)$, and the density is denoted by $\rho(z)$. The P- and S-velocities for a fixed frequency are denoted by $\alpha(z)$ and $\beta(z)$, respectively. As in reference [16], we introduce the functions $\mathscr{H}(z)$, $\mathscr{L}(z)$, and $\varphi(z)$ by

$$\mathscr{H}(z) = \frac{1}{\lambda(z) + 2\mu(z)}, \qquad \mathscr{L}(z) = \frac{\lambda(z)}{\lambda(z) + 2\mu(z)} \tag{2}$$

and

$$\varphi(z) = \frac{4\mu(z)[\lambda(z) + \mu(z)]}{\lambda(z) + 2\mu(z)} = 4\rho(z)\beta^2(z)[1 - \beta^2(z)/\alpha^2(z)]. \tag{3}$$

To allow for a viscoelastic medium, the functions $\lambda(z)$ and $\mu(z)$ may depend on ω. It follows that $\alpha(z)$, $\beta(z)$ and $\mathscr{H}(z)$, $\mathscr{L}(z)$, $\varphi(z)$ may depend on ω as well. The subscript 0 is used to indicate limits as ω tends to zero, and we write $\lambda_0(z)$ and $\mu_0(z)$, for example.

The subscripts F and S are used for fluid and solid regions, respectively. The subscripts L and U are occasionally used for parameters of a lower and an upper boundary condition (or homogeneous half-space), respectively. When the subscript 0 is needed in addition, we write $\varphi_{L,0}$, etc.

Put

$$p = p(\omega, q) = q/\omega, \tag{4}$$

where q is a complex variable. Actually, q coincides with the horizontal wavenumber k. For a fluid region, we will need the propagator matrix $\mathbf{Q}_F(z, \zeta)$

defined by $\mathbf{Q}_F(\zeta, \zeta) = \mathbf{I}$, where $\mathbf{I}$ is the (2×2) identity matrix while z and ζ are depth parameters, and

$$\frac{\partial \mathbf{Q}_F(z, \zeta)}{\partial z} = q \begin{pmatrix} 0 & -\rho^{-1}(z) \\ -\rho(z) & 0 \end{pmatrix} \cdot \mathbf{Q}_F(z, \zeta). \tag{5}$$

For a solid region, we analogously introduce the propagator matrix $\mathbf{Q}_S(z, \zeta)$ defined by $\mathbf{Q}_S(\zeta, \zeta) = \mathbf{I}$, where $\mathbf{I}$ is now the (4×4) identity matrix, and

$$\frac{\partial \mathbf{Q}_S(z, \zeta)}{\partial z} = q \begin{pmatrix} 0 & 1 & \mu_0^{-1}(z) & 0 \\ -\mathscr{L}_0(z) & 0 & 0 & \mathscr{H}_0(z) \\ \varphi_0(z) & 0 & 0 & \mathscr{L}_0(z) \\ 0 & 0 & -1 & 0 \end{pmatrix} \cdot \mathbf{Q}_S(z, \zeta). \tag{6}$$

We will also need the compound matrix $\mathbf{Q}_S(z, \zeta)^{\Lambda_2}$, which is a (6×6) matrix with the (2×2) subdeterminants of $\mathbf{Q}_S(z, \zeta)$ as its elements [18]. It is obvious that $\mathbf{Q}_S(\zeta, \zeta)^{\Lambda_2} = \mathbf{I}$, where $\mathbf{I}$ is the (6×6) identity matrix. The ordinary differential equation (ODE) system satisfied by $\mathbf{Q}_S(z, \zeta)^{\Lambda_2}$ is [17, (3.4)]

$$\frac{\partial [\mathbf{Q}_S(z, \zeta)^{\Lambda_2}]}{\partial z} = q \begin{pmatrix} 0 & 0 & \mathscr{H}_0(z) & -\mu_0^{-1}(z) & 0 & 0 \\ 0 & 0 & \mathscr{L}_0(z) & 1 & 0 & 0 \\ 0 & -1 & 0 & 0 & 1 & \mu_0^{-1}(z) \\ -\varphi_0(z) & -\mathscr{L}_0(z) & 0 & 0 & \mathscr{L}_0(z) & -\mathscr{H}_0(z) \\ 0 & 0 & -\mathscr{L}_0(z) & -1 & 0 & 0 \\ 0 & 0 & \varphi_0(z) & 0 & 0 & 0 \end{pmatrix}$$

$$\cdot [\mathbf{Q}_S(z, \zeta)^{\Lambda_2}]. \tag{7}$$

The elements of $\mathbf{Q}_F(z, \zeta)$, $\mathbf{Q}_S(z, \zeta)$, and $\mathbf{Q}_S(z, \zeta)^{\Lambda_2}$ are apparently entire analytic functions of q.

2.1. THE MODE STRUCTURE

The structure for the class of low-frequency modes such that $\liminf_{\omega \to 0} |k(\omega)| < \infty$ was determined in references [16, 17]. It was shown that $\lim_{\omega \to 0} k(\omega) = q$ always exists for such a mode. Very explicit results for the modes with $q = 0$, finite in number for each particular fluid–solid medium, were provided in references [16; 17, Appendix A]. In particular, six possible asymptotic low-frequency power-law dependencies of $p(\omega)$ on ω were isolated: ω^0, $\omega^{-1/5}$,

$\omega^{-1/3}$, $\omega^{-1/2}$, $\omega^{-3/5}$, and $\omega^{-2/3}$. The modes with non-vanishing low-frequency wavenumber limits q, countably infinite in number for each medium, are in direct one-to-one correspondence with the set of q determined as follows [17, Theorem 5.1 and section 6.1]:

(i) Each interior fluid region F, i.e., a fluid region that is bounded by interfaces to solid regions at depths ζ and z, with $\zeta < z$, contributes with those non-zero q that are zeros for the entire analytic function $(\mathbf{Q}_F(z, \zeta))_{12}$.

(ii) Each interior solid region S, i.e., a solid region that is bounded by interfaces to fluid regions with non-vanishing thickness at depths ζ and z, with $\zeta < z$, contributes with those non-zero q that are zeros for the entire analytic function $(\mathbf{Q}_S(z, \zeta)^{\Delta_2})_{61}$.

(iii) Each remaining fluid (F) or solid (S) region, considered to be an end region, contributes with those non-zero q that are zeros for the appropriate entire analytic function among $\mathbf{Y} \cdot \mathbf{Q}_F(z, \zeta) \cdot \mathbf{X}^{\mathrm{T}}$, $\mathbf{Y} \cdot \mathbf{Q}_S(z, \zeta)^{\Delta_2} \cdot \mathbf{X}^{\mathrm{T}}$, $(\mathbf{Y} \cdot \mathbf{Q}_F(z, \zeta))_2$, $(\mathbf{Y} \cdot \mathbf{Q}_S(z, \zeta)^{\Delta_2})_1$, $(\mathbf{Q}_F(z, \zeta) \cdot \mathbf{X}^{\mathrm{T}})_1$, and $(\mathbf{Q}_S(z, \zeta)^{\Delta_2} \cdot \mathbf{X}^{\mathrm{T}})_6$. Excluding possible homogeneous half-space parts, the region F or S is here assumed to cover the depth interval (ζ, z), where $\zeta < z$. The appropriate lower-end vector $\mathbf{Y}$ or upper-end vector $\mathbf{X}$ is obtained from

$$\mathbf{Y} = q^{-1}(0, 1) \quad \text{(free fluid)},$$

$$\mathbf{Y} = (1, 0) \quad \text{(rigid fluid)},$$

$$\mathbf{Y} = (-\rho_L, \pm 1) \quad \text{(fluid half-space)},$$

$$\mathbf{Y} = q(0, 0, 0, 0, 0, 1) \quad \text{(free solid)},$$

$$\mathbf{Y} = q^{-1}(1, 0, 0, 0, 0, 0) \quad \text{(rigid solid)},$$

$$\mathbf{Y} = (0, 0, 1, 0, 0, 0) \quad \text{(mixed-condition solid)},$$

$$\mathbf{Y} = (0, 0, 0, 1, 0, 0) \quad \text{(solid with vanishing rigid fluid)},$$

$$\mathbf{Y} = q(-\varphi_{L,0}/2, \beta_{L,0}^2/\alpha_{L,0}^2, \mp 1, \pm 1, -\beta_{L,0}^2/\alpha_{L,0}^2, -(\alpha_{L,0}^{-2} + \beta_{L,0}^{-2})/(2\rho_L)) \quad \text{(solid half-space, } ++ \text{ and } -- \text{ sheets)},$$

$$\mathbf{Y} = q^3(8\rho_L\beta_{L,0}^4, 4\beta_{L,0}^2, 0, 0, -4\beta_{L,0}^2, -2/\rho_L) \quad \text{(solid half-space, } -+ \text{ and } +- \text{ sheets)}, \tag{8}$$

or

$$\mathbf{X} = (-1, 0) \quad \text{(free fluid)},$$

$$\mathbf{X} = q(0, 1) \quad \text{(rigid fluid)},$$

$$\mathbf{X} = q(\mp 1, \rho_U) \quad \text{(fluid half-space)},$$

$$\mathbf{X} = q(1, 0, 0, 0, 0, 0) \quad \text{(free solid)},$$

$$\mathbf{X} = q^{-1}(0, 0, 0, 0, 0, 1) \quad \text{(rigid solid)},$$

$$\mathbf{X} = (0, 0, 0, 1, 0, 0) \quad \text{(mixed-condition solid)},$$

$$\mathbf{X} = (0, 0, 1, 0, 0, 0) \quad \text{(solid with vanishing rigid fluid)},$$

$$\mathbf{X} = q(-(\alpha_{U,0}^{-2} + \beta_{U,0}^{-2})/(2\rho_U),\ \beta_{U,0}^2/\alpha_{U,0}^2,\ \mp 1,\ \pm 1,\ -\beta_{U,0}^2/\alpha_{U,0}^2,\ -\varphi_{U,0}/2) \quad \text{(solid half-space, } ++ \text{ and } -- \text{ sheets)},$$

$$\mathbf{X} = q^3(-2/\rho_U,\ 4\beta_{U,0}^2,\ 0,\ 0,\ -4\beta_{U,0}^2,\ 8\rho_U\beta_{U,0}^4) \quad \text{(solid half-space, } -+ \text{ and } +- \text{ sheets)}, \tag{9}$$

respectively.

A number of comments are needed here. For a homogeneous fluid half-space, the upper and lower signs in equations (8) as well as (9) concern the Riemann sheets defined by $R_\alpha(p) = (p^2 - \alpha^{-2})^{1/2} \approx p$ and $R_\alpha(p) \approx -p$, respectively, for large p. For a homogeneous solid half-space, we define four Riemann sheets for large p: $++$ ($R_\alpha(p) \approx R_\beta(p) = (p^2 - \beta^{-2})^{1/2} \approx p$), $-+$ ($-R_\alpha(p) \approx R_\beta(p) \approx p$), $+-$ ($R_\alpha(p) \approx -R_\beta(p) \approx p$), and $--$ ($R_\alpha(p) \approx R_\beta(p) \approx -p$). The corresponding upper and lower signs in equations (8) as well as (9) concern the $++$ and $--$ sheets, respectively. In the presence of one or two homogeneous half-spaces, it should be noted that each of the up to 16 Riemann sheets gets its own modes with non-zero q according to (i)–(iii) above. As detailed in reference [17, section 2], some Riemann sheets may be discarded from consideration.

The powers of q that appear occasionally in equations (8) and (9) may seem superfluous. By keeping track of these (and some other) powers of q, however, the *number* of modes with vanishing low-frequency wavenumber limits can be readily identified according to the argument principle of complex analysis [17, sections 5 and 6.1]. The *total* dispersion function $\mathscr{D}(\omega, p)$ [16] should be considered in this context. Additional powers of q must be included at fluid–solid interfaces [17, section 4.2].

Media with interior fluid regions with vanishing thickness give rise to certain complications as concerns modes with low-frequency wavenumber limits $q \neq 0$ [17, section 6.2], and we have chosen not to include them. There are also certain "exceptional media" with unstable asymptotic low-frequency behaviour for some leaky modes [16, section 7.1; 17, section 6.1 and Appendix A]. However, these media will hardly appear in practice and we ignore to give a detailed discussion.

A key result is that the non-zero low-frequency wavenumber limits q are contributed by each fluid and each solid region taken separately. In effect, each fluid–solid interface is replaced by a two-faced boundary at low frequency, with "rigid" towards the fluid and "free" towards the solid. Accordingly, the low-frequency modes decouple into region-dependent classes, and this classification of modes extends to higher frequencies by continuous mode tracking (section 4).

The proof of this effective medium separation at low frequency was provided in reference [17] by an asymptotic analysis and factorization of the dispersion function. Because of its significance, we include here a heuristic argument as a complement. It will be given in terms of certain transformed displacement-stress vectors (that were also used in reference [17]).

2.2. TRANSFORMED DISPLACEMENT-STRESS VECTORS AND EFFECTIVE MEDIUM SEPARATION AT LOW FREQUENCY

As in reference [19, (7.25) and (7.27)], we write the modal displacement-stress vector as $\mathbf{r}(z) = (r_1(z), r_2(z), r_3(z), r_4(z))^{\mathrm{T}}$. The components of $\mathbf{r}$ concern horizontal displacement, vertical displacement, tangential stress on horizontal planes, and normal stress on horizontal planes, respectively. However, it is often more convenient to use the scaled vector

$$\mathbf{y}(z) = (y_1(z), y_2(z), y_3(z), y_4(z))^{\mathrm{T}} = (\omega r_1(z), \omega r_2(z), r_3(z), r_4(z))^{\mathrm{T}}. \tag{10}$$

For depths z and ζ in the same fluid region F, the field is determined by just two components

$$\mathbf{y}_F(z) = (y_2(z), y_4(z))^{\mathrm{T}} = \mathbf{P}_F(z, \zeta) \cdot \mathbf{y}(\zeta), \tag{11}$$

where $\mathbf{P}_F(z, \zeta)$ is a (2×2) propagator matrix. Assuming that $p \neq 0$, we introduce transformed variables in F according to

$$\mathbf{x}_F = (x_2, x_4)^{\mathrm{T}} = \mathrm{diag}(1, p) \cdot \mathbf{y}_F. \tag{12}$$

It follows from reference [16, (2.10–11)] that

$$\mathbf{x}_F'(z) = \omega p \begin{pmatrix} 0 & p^{-2}\mathscr{H}(z) - \rho^{-1}(z) \\ -\rho(z) & 0 \end{pmatrix} \cdot \mathbf{x}_F(z). \tag{13}$$

Letting ω tend to zero in such a way that $q = \omega p \neq 0$ is fixed, the ODE system (5), defining the propagator matrix $\mathbf{Q}_F$, is obtained.

For depths z and ζ in the same solid region S, one needs all four components of

$$\mathbf{y}_S(z) = \mathbf{y}(z) = \mathbf{P}_S(z, \zeta) \cdot \mathbf{y}(\zeta), \tag{14}$$

where $\mathbf{P}_S(z, \zeta)$ is a (4×4) propagator matrix. Assuming that $p \neq 0$, we now introduce transformed variables in S according to

$$\mathbf{x}_S = \mathrm{diag}(p, p, 1, 1) \cdot \mathbf{y}_S. \tag{15}$$

It follows from reference [16, (2.12–13)] that

$$\mathbf{x}'_S(z) = \omega p \begin{pmatrix} 0 & 1 & \mu^{-1}(z) & 0 \\ -\mathscr{L}(z) & 0 & 0 & \mathscr{H}(z) \\ \varphi(z) - p^{-2}\rho(z) & 0 & 0 & \mathscr{L}(z) \\ 0 & -p^{-2}\rho(z) & -1 & 0 \end{pmatrix} \cdot \mathbf{x}_S(z). \tag{16}$$

Letting ω tend to zero in such a way that $q = \omega p \neq 0$ is fixed, the ODE system (6), defining the propagator matrix $\mathbf{Q}_S$, is obtained.

We are now in a position to assess the behaviour at a fluid–solid interface, between fluid region F and solid region S, as ω tends to zero in such a way that $q = \omega p \neq 0$ is fixed. Since the y_2 and y_4 variables are continuous across the interface, it follows from equations (12) and (15) that

$$\text{“fluid-side } x_2\text{”} = p^{-1} \text{ “solid-side } x_2\text{”}, \tag{17}$$

$$\text{“solid-side } x_4\text{”} = p^{-1} \text{ “fluid-side } x_4\text{”} \tag{18}$$

at the interface. The effective low-frequency interface conditions that develop are indeed those prescribed by a separating two-faced boundary that is “rigid” towards the fluid and “free” towards the solid. (Note that p tends to infinity as ω tends to zero, according to our assumptions).

One can now understand how the mode-structure rules appear that were formulated in section 2.1. The solid case, involving compound matrices, may require some further comment, however. Consider a solid region S between depths ζ and z, $\zeta < z$, where (effective) boundary conditions for $\mathbf{x}_S$ are specified: $\mathbf{G}_{Ux} \cdot \mathbf{x}_S(\zeta) = \mathbf{0}$ and $\mathbf{G}_{Lx} \cdot \mathbf{x}_S(z) = \mathbf{0}$, where $\mathbf{G}_{Ux}$ and $\mathbf{G}_{Lx}$ are certain (2×4) matrices. The condition for a corresponding low-frequency modal wavenumber limit q coincides with the condition for a non-trivial solution $\mathbf{x}_S$, i.e.,

$$\det \begin{pmatrix} \mathbf{G}_{Ux} \\ \mathbf{G}_{Lx} \cdot \mathbf{Q}_S(z, \zeta) \end{pmatrix} = 0, \tag{19}$$

where the relation $\mathbf{x}_S(z) = \mathbf{Q}_S(z, \zeta) \cdot \mathbf{x}_S(\zeta)$ has been used. Applying Laplace's development of a (4×4) determinant in terms of (2×2) subdeterminants, and some compound-matrix algebra [18], equation (19) can be reformulated as

$$\mathbf{Y} \cdot \mathbf{Q}_S(z, \zeta)^{\Lambda_2} \cdot \mathbf{X}^{\mathrm{T}} = 0, \tag{20}$$

where $\mathbf{Y} = (\mathbf{G}_{Lx})^{\Lambda_2}$ and $\mathbf{X} = [(\mathbf{G}_{Ux})^{\Lambda_2}]_{anti}$, see reference [18, section 3].

3. NUMERICAL DETERMINATION OF THE LOW-FREQUENCY WAVENUMBER LIMITS q

It follows from the mode-structure results in section 2.1 that a numerical determination of the low-frequency modal wavenumber limits q boils down to numerical determination of the zeros for certain entire analytic functions. We will use adaptive winding-number integral techniques for locating such zeros in an efficient and reliable manner; see reference [20] for a description of our particular algorithm. It is essential, however, that the analytic functions can be evaluated efficiently at arbitrary points. For this purpose, a restriction to homogeneously layered media is most useful (at least for the solid regions).

Now, it is well-known that the propagator matrices for homogeneous layers can be given explicitly. Such explicit expressions for $\mathbf{P}_F$, $\mathbf{P}_S$, and $\mathbf{P}_S^{\Lambda_2}$ can be found in references [21, (35)], [22, (4)], and [21, (13)], respectively. For a whole fluid or solid region composed of homogeneous layers, the "total" propagator matrix is subsequently obtained by multiplication of the propagator matrices of the individual layers.

According to the variable transformations that were introduced in section 2.2, we may write

$$\mathbf{Q}_F(q) = \lim_{\omega \to 0} \operatorname{diag}(1, p) \cdot \mathbf{P}_F(\omega, p) \cdot \operatorname{diag}(1, p^{-1}), \tag{21}$$

$$\mathbf{Q}_S(q) = \lim_{\omega \to 0} \operatorname{diag}(p, p, 1, 1) \cdot \mathbf{P}_S(\omega, p) \cdot \operatorname{diag}(p^{-1}, p^{-1}, 1, 1), \tag{22}$$

$$\mathbf{Q}_S^{\Lambda_2}(q) = \lim_{\omega \to 0} \operatorname{diag}(p, 1, 1, 1, 1, p^{-1}) \cdot \mathbf{P}_S^{\Lambda_2}(\omega, p) \cdot \operatorname{diag}(p^{-1}, 1, 1, 1, 1, p), \tag{23}$$

where the zero-frequency limit is approached in such a way that $p = q/\omega$ tends to ∞ (for fixed q).

For the rest of this section, we consider a homogeneous layer between depths ζ and z, with $\zeta < z$. We put $d = z - \zeta$ and understand that all propagator matrices are taken "from ζ to z". Hence, $\mathbf{Q}_F$ means $\mathbf{Q}_F(z, \zeta)$, etc. The arguments q, or ω, p, are also omitted for brevity. By equation (21) and reference [21, (35)], it readily follows that

$$\mathbf{Q}_F = \begin{pmatrix} \cosh(qd) & -\rho^{-1} \sinh(qd) \\ -\rho \sinh(qd) & \cosh(qd) \end{pmatrix}. \tag{24}$$

In fact, it is here only essential that the density ρ is constant throughout the layer, while the medium velocity α_0 may vary with depth (it does not appear in the ODE system (5)).

Concerning $\mathbf{Q}_S$ and $\mathbf{Q}_S^{A_2}$, the expressions [22, (4)] and [21, (13)] are not convenient for letting ω tend to zero in the way prescribed by equations (22) and (23). Instead, we apply the alternative expressions (38) and (31)–(34) in reference [21], that were derived there for numerical purposes. For the elements of $\mathbf{Q}_S$, we get in this way

$$
\begin{aligned}
(Q_S)_{11} &= \cosh(qd) + (1 - \beta_0^2 \alpha_0^{-2})\, qd \sinh(qd),\\
(Q_S)_{22} &= \cosh(qd) - (1 - \beta_0^2 \alpha_0^{-2})\, qd \sinh(qd),\\
(Q_S)_{13} &= [(\beta_0^{-2} - \alpha_0^{-2})\, qd \cosh(qd) + (\beta_0^{-2} + \alpha_0^{-2}) \sinh(qd)]/(2\rho),\\
(Q_S)_{24} &= [-(\beta_0^{-2} - \alpha_0^{-2})\, qd \cosh(qd) + (\beta_0^{-2} + \alpha_0^{-2}) \sinh(qd)]/(2\rho),\\
(Q_S)_{12} &= (1 - \beta_0^2 \alpha_0^{-2})\, qd \cosh(qd) + \beta_0^2 \alpha_0^{-2} \sinh(qd),\\
(Q_S)_{21} &= -(1 - \beta_0^2 \alpha_0^{-2})\, qd \cosh(qd) + \beta_0^2 \alpha_0^{-2} \sinh(qd),\\
(Q_S)_{14} &= (\beta_0^{-2} - \alpha_0^{-2})\, qd \sinh(qd)/(2\rho),\\
(Q_S)_{32} &= 2\rho\beta_0^2 (1 - \beta_0^2 \alpha_0^{-2})\, qd \sinh(qd),\\
(Q_S)_{31} &= 2\rho\beta_0^2 (1 - \beta_0^2 \alpha_0^{-2})[qd \cosh(qd) + \sinh(qd)],\\
(Q_S)_{42} &= 2\rho\beta_0^2 (1 - \beta_0^2 \alpha_0^{-2})[-qd \cosh(qd) + \sinh(qd)].
\end{aligned}
\tag{25}
$$

For the remaining elements of $\mathbf{Q}_S$, we have the simple relations $(Q_S)_{23} = -(Q_S)_{14}$, $(Q_S)_{33} = (Q_S)_{11}$, $(Q_S)_{34} = -(Q_S)_{21}$, $(Q_S)_{41} = -(Q_S)_{32}$, $(Q_S)_{43} = -(Q_S)_{12}$, and $(Q_S)_{44} = (Q_S)_{22}$.

The elements of $\mathbf{Q}_S^{A_2}$ become

$$
\begin{aligned}
(\mathbf{Q}_S^{A_2})_{13} &= [(\beta_0^{-2} + \alpha_0^{-2}) \cosh(qd) \sinh(qd) - (\beta_0^{-2} - \alpha_0^{-2})\, qd]/(2\rho),\\
(\mathbf{Q}_S^{A_2})_{14} &= -[(\beta_0^{-2} + \alpha_0^{-2}) \cosh(qd) \sinh(qd) + (\beta_0^{-2} - \alpha_0^{-2})\, qd]/(2\rho),\\
(\mathbf{Q}_S^{A_2})_{23} &= -\beta_0^2 \alpha_0^{-2} \cosh(qd) \sinh(qd) + (1 - \beta_0^2 \alpha_0^{-2})\, qd,\\
(\mathbf{Q}_S^{A_2})_{24} &= \beta_0^2 \alpha_0^{-2} \cosh(qd) \sinh(qd) + (1 - \beta_0^2 \alpha_0^{-2})\, qd,
\end{aligned}
$$

$$(\mathbf{Q}_S^{\Delta_2})_{31} = 2\rho\beta_0^2(1-\beta_0^2\alpha_0^{-2})\,[\cosh(qd)\sinh(qd) - qd],$$

$$(\mathbf{Q}_S^{\Delta_2})_{41} = -2\rho\beta_0^2(1-\beta_0^2\alpha_0^{-2})\,[\cosh(qd)\sinh(qd) + qd],$$

$$(\mathbf{Q}_S^{\Delta_2})_{16} = [(\beta_0^{-2}+\alpha_0^{-2})^2\sinh^2(qd) - (\beta_0^{-2}-\alpha_0^{-2})^2(qd)^2]/(4\rho^2),$$

$$(\mathbf{Q}_S^{\Delta_2})_{61} = 4\rho^2\beta_0^4(1-\beta_0^2\alpha_0^{-2})^2\,[\sinh^2(qd) - (qd)^2],$$

$$(\mathbf{Q}_S^{\Delta_2})_{33} = \cosh^2(qd),$$

$$(\mathbf{Q}_S^{\Delta_2})_{34} = -\sinh^2(qd),$$

$$(\mathbf{Q}_S^{\Delta_2})_{43} = -\sinh^2(qd),$$

$$(\mathbf{Q}_S^{\Delta_2})_{11} = 1 + (1-\beta_0^4\alpha_0^{-4})\sinh^2(qd) + (1-\beta_0^2\alpha_0^{-2})^2(qd)^2,$$

$$(\mathbf{Q}_S^{\Delta_2})_{22} = 1 + \beta_0^4\alpha_0^{-4}\sinh^2(qd) - (1-\beta_0^2\alpha_0^{-2})^2(qd)^2,$$

$$(\mathbf{Q}_S^{\Delta_2})_{12} = -[\beta_0^2\alpha_0^{-2}(\beta_0^{-2}+\alpha_0^{-2})\sinh^2(qd) - \beta_0^{-2}(1-\beta_0^2\alpha_0^{-2})^2(qd)^2]/(2\rho),$$

$$(\mathbf{Q}_S^{\Delta_2})_{21} = -2\rho\beta_0^2(1-\beta_0^2\alpha_0^{-2})[\beta_0^2\alpha_0^{-2}\sinh^2(qd) + (1-\beta_0^2\alpha_0^{-2})(qd)^2]. \tag{26}$$

The list is completed by the simple relations $(\mathbf{Q}_S^{\Delta_2})_{66} = (\mathbf{Q}_S^{\Delta_2})_{11}$, $-(\mathbf{Q}_S^{\Delta_2})_{15} = (\mathbf{Q}_S^{\Delta_2})_{26} = -(\mathbf{Q}_S^{\Delta_2})_{56} = (\mathbf{Q}_S^{\Delta_2})_{12}$, $(\mathbf{Q}_S^{\Delta_2})_{46} = -(\mathbf{Q}_S^{\Delta_2})_{13}$, $(\mathbf{Q}_S^{\Delta_2})_{36} = -(\mathbf{Q}_S^{\Delta_2})_{14}$, $-(\mathbf{Q}_S^{\Delta_2})_{51} = (\mathbf{Q}_S^{\Delta_2})_{62} = -(\mathbf{Q}_S^{\Delta_2})_{65} = (\mathbf{Q}_S^{\Delta_2})_{21}$, $(\mathbf{Q}_S^{\Delta_2})_{25} = (\mathbf{Q}_S^{\Delta_2})_{52} = 1 - (\mathbf{Q}_S^{\Delta_2})_{22}$, $(\mathbf{Q}_S^{\Delta_2})_{55} = (\mathbf{Q}_S^{\Delta_2})_{22}$, $-(\mathbf{Q}_S^{\Delta_2})_{53} = -(\mathbf{Q}_S^{\Delta_2})_{42} = (\mathbf{Q}_S^{\Delta_2})_{45} = (\mathbf{Q}_S^{\Delta_2})_{23}$, $-(\mathbf{Q}_S^{\Delta_2})_{32} = (\mathbf{Q}_S^{\Delta_2})_{35} = -(\mathbf{Q}_S^{\Delta_2})_{54} = (\mathbf{Q}_S^{\Delta_2})_{24}$, $(\mathbf{Q}_S^{\Delta_2})_{64} = -(\mathbf{Q}_S^{\Delta_2})_{31}$, $(\mathbf{Q}_S^{\Delta_2})_{44} = (\mathbf{Q}_S^{\Delta_2})_{33}$, and $(\mathbf{Q}_S^{\Delta_2})_{63} = -(\mathbf{Q}_S^{\Delta_2})_{41}$.

In analogy to reference [21, (14)–(15)], we may note that

$$(\mathbf{Q}_S^{\Delta_2})_{16} = -4\underline{(\mathbf{Q}_S^{\Delta_2})_{13}}\,\underline{(\mathbf{Q}_S^{\Delta_2})_{14}} = -4\underline{(\mathbf{Q}_S^{\Delta_2})_{36}}\,\underline{(\mathbf{Q}_S^{\Delta_2})_{46}}, \tag{27}$$

$$(\mathbf{Q}_S^{\Delta_2})_{61} = -4\underline{(\mathbf{Q}_S^{\Delta_2})_{63}}\,\underline{(\mathbf{Q}_S^{\Delta_2})_{64}} = -4\underline{(\mathbf{Q}_S^{\Delta_2})_{31}}\,\underline{(\mathbf{Q}_S^{\Delta_2})_{41}}, \tag{28}$$

where an underlined quantity is to be evaluated with d replaced by $d/2$ in equation (26).

For a homogeneous solid plate with free boundaries, the simple equations (1) are obtained directly from our expression for $(\mathbf{Q}_S^{\Delta_2})_{61}$. (For another derivation, using l'Hôpital's rule, see reference [7, section 6.8]. We realize that the independence of α_0 and β_0 is lost in other cases, for example when the plate is rigidly held and the expression for $(\mathbf{Q}_S^{\Delta_2})_{16}$ becomes relevant.

3.1. PROPAGATOR-MATRIX FACTORIZATION FOR ENHANCED COMPUTATIONAL EFFICIENCY

In references [22, 23], we advocated matrix factorization techniques to speed up propagator computations for homogeneously layered media. The basic idea is to write the propagator matrix for each layer as a product of *sparse* matrices, which can be applied in sequence to the vector being propagated (a row vector from the left or a column vector from the right). A useful factorization of this type for the expression of $\mathbf{Q}_F$ according to equation (24) is

$$\mathbf{Q}_F = \frac{1}{2}\,\mathrm{diag}(1, \rho)\begin{pmatrix} 1 & 1 \\ -1 & 1 \end{pmatrix}\mathrm{diag}(\mathrm{e}^{qd}, \mathrm{e}^{-qd})\begin{pmatrix} 1 & -1 \\ 1 & 1 \end{pmatrix}\mathrm{diag}(1, \rho^{-1}). \tag{29}$$

It is readily derived from the definitions of the hyperbolic functions.

A factorization of $\mathbf{Q}_S$ is not as apparent, but it can be obtained by standard ODE system techniques, involving a Jordan decomposition of the degenerate system matrix appearing in equation (6). We may write

$$\begin{pmatrix} 0 & 1 & \mu_0^{-1}(z) & 0 \\ -\mathscr{L}_0(z) & 0 & 0 & \mathscr{H}_0(z) \\ \varphi_0(z) & 0 & 0 & \mathscr{L}_0(z) \\ 0 & 0 & -1 & 0 \end{pmatrix} = \mathbf{T}^{-1}\cdot\mathbf{J}\cdot\mathbf{T}, \tag{30}$$

where

$$\mathbf{J} = \begin{pmatrix} 1 & 2 & 0 & 0 \\ 0 & 1 & 0 & 0 \\ 0 & 0 & -1 & 0 \\ 0 & 0 & -2 & -1 \end{pmatrix} \tag{31}$$

corresponding to the multiple and degenerate eigenvalues ± 1, and

$$\mathbf{T} = \frac{1}{2(1+\theta)}\begin{pmatrix} 1 & -1 & \theta & -\theta \\ 1 & 1 & 1 & 1 \\ -1 & 1 & 1 & -1 \\ -1 & -1 & \theta & \theta \end{pmatrix}\mathrm{diag}(1, 1, (2\mu_0)^{-1}, (2\mu_0)^{-1}), \tag{32}$$

$$\mathbf{T}^{-1} = \mathrm{diag}(1, 1, 2\mu_0, 2\mu_0)\begin{pmatrix} 1 & \theta & -\theta & -1 \\ -1 & \theta & \theta & -1 \\ 1 & 1 & 1 & 1 \\ -1 & 1 & -1 & 1 \end{pmatrix} \tag{33}$$

are variable-transformation matrices. The layer parameter θ is defined by $\theta = 1 + 2\mu_0/(\lambda_0 + \mu_0)$. Among the possible representations of Jordan type, we have taken care to choose one for which the useful antisymmetry property "$Y_5 = -Y_2$" [22, (9)] can be maintained during the implied compound-matrix propagation (see below).

The propagator matrix $\mathbf{U}$ for the simple four-dimensional ODE system $\mathbf{u}' = q\mathbf{J}\cdot\mathbf{u}$, given in terms of the vector function $\mathbf{u}(z) = (u_1(z), u_2(z), u_3(z), u_4(z))^{\mathrm{T}}$, can be written

$$\mathbf{U} = \begin{pmatrix} 1 & 2qd & 0 & 0 \\ 0 & 1 & 0 & 0 \\ 0 & 0 & 1 & 0 \\ 0 & 0 & -2qd & 1 \end{pmatrix} \operatorname{diag}(e^{qd}, e^{qd}, e^{-qd}, e^{-qd}) \tag{34}$$

and $\mathbf{Q}_S$ may be factorized as

$$\mathbf{Q}_S = \mathbf{T}^{-1}\cdot\mathbf{U}\cdot\mathbf{T}. \tag{35}$$

Extending the factorizations of $\mathbf{T}$ and $\mathbf{T}^{-1}$ slightly, we finally obtain

$$\begin{aligned} \mathbf{Q}_S = \operatorname{diag}(1, 1, 2\mu_0, 2\mu_0) & \begin{pmatrix} 1 & 1 & 0 & 0 \\ -1 & 1 & 0 & 0 \\ 0 & 0 & 1 & 1 \\ 0 & 0 & -1 & 1 \end{pmatrix} \begin{pmatrix} 1 & 0 & -\theta & 0 \\ 0 & \theta & 0 & -1 \\ 1 & 0 & 1 & 0 \\ 0 & 1 & 0 & 1 \end{pmatrix} \\ \times & \begin{pmatrix} 1 & 2qd & 0 & 0 \\ 0 & 1 & 0 & 0 \\ 0 & 0 & 1 & 0 \\ 0 & 0 & -2qd & 1 \end{pmatrix} \operatorname{diag}(e^{qd}, e^{qd}, e^{-qd}, e^{-qd}) \\ \times & \frac{1}{2(1+\theta)} \begin{pmatrix} 1 & 0 & \theta & 0 \\ 0 & 1 & 0 & 1 \\ -1 & 0 & 1 & 0 \\ 0 & -1 & 0 & \theta \end{pmatrix} \begin{pmatrix} 1 & -1 & 0 & 0 \\ 1 & 1 & 0 & 0 \\ 0 & 0 & 1 & -1 \\ 0 & 0 & 1 & 1 \end{pmatrix} \\ \times & \operatorname{diag}(1, 1, (2\mu_0)^{-1}, (2\mu_0)^{-1}). \end{aligned} \tag{36}$$

Of course, we would recover equations (25) by multiplying together the factor matrices. Note that

$$1 - \beta_0^2\alpha_0^{-2} = \frac{2}{1+\theta} \quad \text{and} \quad 1 + \beta_0^2\alpha_0^{-2} = \frac{2\theta}{1+\theta}. \tag{37}$$

Since the compound matrix of a product is equal to the product of the individual compound matrices, equation (36) provides an obvious starting point for decomposing $\mathbf{Q}_S^{\Lambda_2}$. With some additional decomposition we arrive at

$$\mathbf{Q}_S^{\Lambda_2} = \operatorname{diag}(1, 2\mu_0, 2\mu_0, 2\mu_0, 2\mu_0, 4\mu_0^2)$$

$$\times \begin{pmatrix} 1 & 0 & 0 & 0 & 0 & 0 \\ 0 & 1 & 0 & 0 & 0 & 0 \\ 0 & 0 & 1 & 1 & 0 & 0 \\ 0 & 0 & -1 & 1 & 0 & 0 \\ 0 & 0 & 0 & 0 & 1 & 0 \\ 0 & 0 & 0 & 0 & 0 & 1 \end{pmatrix} \begin{pmatrix} 2 & 0 & 0 & 0 & 0 & 0 \\ 0 & 1 & 1 & 1 & 1 & 0 \\ 0 & 0 & 1 & -1 & 0 & 0 \\ 0 & -1 & 0 & 0 & 1 & 0 \\ 0 & 1 & -1 & -1 & 1 & 0 \\ 0 & 0 & 0 & 0 & 0 & 2 \end{pmatrix}$$

$$\times \begin{pmatrix} \theta & 0 & -1 & 0 & 0 & 0 \\ 0 & 1 & 0 & 0 & 0 & 0 \\ 1 & 0 & 1 & 0 & 0 & 0 \\ 0 & 0 & 0 & \theta & 0 & 1 \\ 0 & 0 & 0 & 0 & 1 & 0 \\ 0 & 0 & 0 & -1 & 0 & 1 \end{pmatrix} \begin{pmatrix} 1 & 0 & 0 & \theta & 0 & 0 \\ 0 & 1+\theta & 0 & 0 & 0 & 0 \\ 0 & 0 & 1 & 0 & 0 & -\theta \\ -1 & 0 & 0 & 1 & 0 & 0 \\ 0 & 0 & 0 & 0 & 1+\theta & 0 \\ 0 & 0 & 1 & 0 & 0 & 1 \end{pmatrix}$$

$$\times \begin{pmatrix} 1 & 0 & 0 & 0 & 0 & 0 \\ 0 & 1 & 0 & 2qd & 0 & 0 \\ 0 & -2qd & 1 & -4q^2d^2 & 2qd & 0 \\ 0 & 0 & 0 & 1 & 0 & 0 \\ 0 & 0 & 0 & -2qd & 1 & 0 \\ 0 & 0 & 0 & 0 & 0 & 1 \end{pmatrix} \operatorname{diag}(\mathrm{e}^{2qd}, 1, 1, 1, 1, \mathrm{e}^{-2qd}) \tag{38}$$

$$\times \frac{1}{4(1+\theta)^2} \begin{pmatrix} 1 & 0 & 1 & 0 & 0 & 0 \\ 0 & 1 & 0 & 0 & 0 & 0 \\ -1 & 0 & \theta & 0 & 0 & 0 \\ 0 & 0 & 0 & 1 & 0 & -1 \\ 0 & 0 & 0 & 0 & 1 & 0 \\ 0 & 0 & 0 & 1 & 0 & \theta \end{pmatrix} \begin{pmatrix} 1 & 0 & 0 & -\theta & 0 & 0 \\ 0 & 1+\theta & 0 & 0 & 0 & 0 \\ 0 & 0 & 1 & 0 & 0 & \theta \\ 1 & 0 & 0 & 1 & 0 & 0 \\ 0 & 0 & 0 & 0 & 1+\theta & 0 \\ 0 & 0 & -1 & 0 & 0 & 1 \end{pmatrix}$$

$$\times \begin{pmatrix} 1 & 0 & 0 & 0 & 0 & 0 \\ 0 & 1 & 0 & 0 & 0 & 0 \\ 0 & 0 & 1 & 1 & 0 & 0 \\ 0 & 0 & -1 & 1 & 0 & 0 \\ 0 & 0 & 0 & 0 & 1 & 0 \\ 0 & 0 & 0 & 0 & 0 & 1 \end{pmatrix} \begin{pmatrix} 2 & 0 & 0 & 0 & 0 & 0 \\ 0 & 1 & -1 & -1 & 1 & 0 \\ 0 & 0 & 1 & -1 & 0 & 0 \\ 0 & 1 & 0 & 0 & -1 & 0 \\ 0 & 1 & 1 & 1 & 1 & 0 \\ 0 & 0 & 0 & 0 & 0 & 2 \end{pmatrix}$$

$$\times \operatorname{diag}(1, (2\mu_0)^{-1}, (2\mu_0)^{-1}, (2\mu_0)^{-1}, (2\mu_0)^{-1}, (4\mu_0^2)^{-1}).$$

Care has here been taken to maintain the useful antisymmetry property "$Y_5 = -Y_2$" [22, (9)] during the sequence of sparse-matrix multiplications that arise when a row vector $\mathbf{Y} = (Y_1, Y_2, Y_3, Y_4, Y_5, Y_6)$ is propagated from the left. It is in general necessary to apply some scaling of the diagonal matrix involving the exponentials in order to avoid overflow, cf. reference [22, section 5]. The sequential application of equation (38) is much more efficient and convenient than a direct multiplication using equations (26)–(28).

The asymptotic mode shapes $\mathbf{x}_F$ (for a fluid region) and $\mathbf{x}_S$ (for a solid region) may be computed by compound-matrix stabilization techniques as suggested in reference [24, section 4.1]. It is easily realized that "back-propagation in large steps", according to reference [18, Appendix A], is feasible in connection with the non-diagonal matrix $\mathbf{U}$ of (34) as well.

4. IMPLIED MODE STRUCTURE AT HIGHER FREQUENCIES BY MODE TRACKING

It follows from the results and techniques of sections 2 and 3 how the low-frequency mode structure can be determined for each particular fluid–solid medium, including all modes for which $\liminf_{\omega \to 0} |k(\omega)| < \infty$. By tracking continuous mode trajectories, for increasing frequency, the low-frequency mode structure can apparently be carried to higher frequencies. A given mode at high frequency may conversely be connected to its low-frequency "origin" by tracking the corresponding $p(\omega)$ or $k(\omega)$ for decreasing ω. It is convenient to combine the winding-number integral algorithm of reference [20] with a simple procedure to step out in frequency utilizing $p'(\omega)$ or the group slowness $k'(\omega) = p(\omega) + \omega p'(\omega)$, which can be conveniently computed [24]. With confidence in these numerical techniques, it is in fact easy to verify that a modal slowness $p(\omega)$ is *exactly* on the real or imaginary axis. We obtain the number of modal slowness within small rectangles, according to the argument principle, and an isolated modal slowness close to the axes must typically be *on* the axes, since off-axes p do in general appear in pairs (p and its complex conjugate $\bar{p}$, or p and $-\bar{p}$) according to symmetry arguments for the dispersion function $D(\omega, p)$.

At very low frequencies, the mentioned mode tracking may run into problems. Numerical precision may be lost by cancellation effects when individual propagator-matrix elements are formed according to the usual compound-matrix

formulas for homogeneously layered media. Alternative, cancellation-free, expressions are needed under these circumstances. The expressions derived in reference [21], for application to slow-mode computations, turn out to be adequate, see Appendix A.

Some further mode-tracking problems, that we wish to address in this section, concern the passage of double roots (for p or k, at a fixed positive ω) and branch points (in the presence of homogeneous half-spaces). Until further notice in section 4.4, we assume that the medium is absorption-free with real medium slownesses. In addition, homogeneous half-spaces are excluded in section 4.1.

4.1. PASSAGE OF DOUBLE ROOTS FOR A MEDIUM WITHOUT HOMOGENEOUS HALF-SPACES

At each frequency, the modal slownesses p appear in pairs, since p and $-p$ appear simultaneously. Off-axes modal slownesses even appear in quartets in the absorption-free case, since $p, \bar{p}, -\bar{p}, -p$ (where the complex conjugate is denoted by a bar) appear simultaneously under these circumstances. (The dispersion function $D(\omega, p)$ will be real-valued for real, and imaginary, p. It is also analytic in p, for each ω.)

It follows that a modal slowness at the origin must be a double root. The simplest examples are provided by all-fluid media, for which the modal slownesses are confined to the axes. When ω is decreased through a cut-off frequency ω_c, the corresponding modal slowness p moves from the real axis to the imaginary axis (e.g., reference [2, section 5.4]). The power expansion of $D(\omega, p)$ at ω_c, $p_c = 0$ starts with some multiple of $p^2 - \gamma_c(\omega - \omega_c)$, where γ_c is a positive constant [25, section 3.1], which determines the behaviour of $p(\omega)$ for ω close to ω_c.

The low-frequency modal wavenumber limits $q \neq 0$ contributed by the solid regions in a medium will typically be complex, off the axes. This is indeed the case for a homogeneous solid plate with free boundaries, according to the simple equations (1). The off-axes q appear in quartets in the absorption-free case: as $q, \bar{q}, -\bar{q}, -q$. In order to produce such a combination at low frequency, *two* pairs of real high-frequency modal slownesses $p_1, -p_1$ and $p_2, -p_2$ must combine. The way they may combine is by forming a double root somewhere on the axes. For an example, see reference [25, section 3.4].

The typical behaviour at a multiple root p_0 at ω_0 is that "stars" are formed on entry to and exit from p_0. This follows from general considerations of $D(\omega, p)$ as an analytic function of p for each ω, e.g., references [8, p. 171; 25, Proposition 1].

4.2. PASSAGE OF BRANCH POINTS FOR A MEDIUM WITH HOMOGENEOUS HALF-SPACES

In the presence of one or two homogeneous half-spaces, we agree to define Riemann sheets as follows (cf. the paragraph following equations (8) and (9)). For a homogeneous fluid half-space with slowness α^{-1}, a $+$ sheet is defined by $R_\alpha(p) = (p^2 - \alpha^{-2})^{1/2} = p\sqrt{1 - \alpha^{-2}p^{-2}}$ and a $-$ sheet is defined by $R_\alpha(p) = -p\sqrt{1 - \alpha^{-2}p^{-2}}$. Here, the square root $\sqrt{\ }$ is chosen according to its principal branch with $-\pi/2 < \arg(\sqrt{\ }) \leqslant \pi/2$.

For a homogeneous solid half-space with P- and S-slownesses α^{-1} and β^{-1}, a $++$ sheet is analogously defined by $R_\alpha(p) = p\sqrt{1-\alpha^{-2}p^{-2}}$ and $R_\beta(p) = (p^2-\beta^{-2})^{1/2} = p\sqrt{1-\beta^{-2}p^{-2}}$. Three other sheets, $-+$, $+-$, and $--$, are introduced in the obvious way with "$R_\alpha(p)$" specified before "$R_\beta(p)$".

These particular Riemann sheets are perfectly adapted to a study of modes for large p, since the branch cuts will be bounded arcs connecting positive and negative branch points, and each $R_\alpha(p)$ or $R_\beta(p)$ will be analytic for all large p. It should be noted that if p is a modal slowness, $-p$ will be a modal slowness on the "opposite" sheet ($-$ instead of $+$, $+-$ instead of $-+$, etc.). In the absorption-free case, the modal slownesses p and $\bar{p}$ appear simultaneously on the same sheet, since the analytic dispersion function $D(\omega, p)$ will be real-valued for large real p. These rules are quite useful. The "physical sheet" will agree with the $+$ (or $++$) sheet in the right half-plane and with the $-$ (or $--$) sheet in the left half-plane.

Except for media with low-velocity half-spaces, modal slowness trajectories $p(\omega)$ will typically hit the branch point with the largest slowness. (The mirror branch point on the negative axis will of course also be involved). For definiteness, we assume that this branch point with the largest slowness is an S-wave branch point for a lower homogeneous solid half-space, and we denote it by β_L^{-1}. The key observation now is that, by isolating $R_{\beta_L}(p)$, the dispersion function $D(\omega, p)$ can be expressed as

$$D(\omega, p) = A(\omega, p)\, R_{\beta_L}(p) + B(\omega, p), \tag{39}$$

where $A(\omega, p)$, $B(\omega, p)$ are new "dispersion-like" functions only involving branch points with magnitude smaller than β_L^{-1}. This follows directly from reference [16, (2.19)]. In the absorption-free case, $A(\omega, p)$ and $B(\omega, p)$ will both be real-valued (and regular) for real p in a neighbourhood of β_L^{-1}. When there are lower velocities than β_L in the medium, giving $B(\omega, \beta_L^{-1})$ an oscillating character as ω is varied, the branch point β_L^{-1} will be hit for frequencies ω_b such that $B(\omega_b, \beta_L^{-1}) = 0$. Assuming $A(\omega_b, \beta_L^{-1}) \neq 0$ and $(\partial B/\partial\omega)(\omega_b, \beta_L^{-1}) \neq 0$, which is the typical case, it follows that the mode trajectory $p(\omega)$ for ω close to ω_b is real with

$$R_{\beta_L}(p(\omega)) \approx (\omega - \omega_b)\, T, \tag{40}$$

where $T = -(\partial B/\partial\omega)(\omega_b, \beta_L^{-1})/A(\omega_b, \beta_L^{-1})$. In particular,

$$p(\omega) \approx \beta_L^{-1} + (\omega - \omega_b)^2\, T^2 \beta_L/2 \tag{41}$$

and $p(\omega)$ will "bounce out" and change Riemann sheets when ω passes through ω_b. The behaviour is related to the approach of a pure branch point limit slowness as considered in reference [16, section 4.1].

As will be seen in section 6, the typical mechanism for entering real modal slownesses $p(\omega)$ from the physical sheet into the complex plane, as ω is decreased, appears to be the following. At first, the branch point with maximum slowness is hit (according to equation (41), for example) and the Riemann sheet is changed. As ω is

decreased further, the real $p(\omega)$ increases until it collides with another mode slowness trajectory that has resided on the present leaky Riemann sheet all the time. A double root is formed and both modal slownesses leave the real axis, initially in the orthogonal direction, as complex conjugate numbers. This mechanism appears to be typical for homogeneous fluid as well as solid half-spaces, simple Pekeris waveguides included [2, section 2.4.5]. (It might appear from reference [2, p. 127] that $p(\omega)$ would leave the real axis already at the branch point, but this is not the case.)

A fifth double-root type of example is obtained in this way, in addition to the four examples in reference [25]. However, it may also happen that a mode proceeds along the positive real slowness axis, on a non-physical sheet after having hit the branch point, in such a way that the wavenumber $k(\omega)$ tends to a real q as ω tends to zero. We do not know if positive real wavenumber limits q are possible on the physical sheet.

It should be observed that branch points with smaller magnitude will typically not be hit exactly. In the present context, for example, with a lower homogeneous solid half-space, an isolation of $R_{\alpha_L}(p)$ according to $D(\omega, p) = A_1(\omega, p)R_{\alpha_L}(p) + B_1(\omega, p)$ will imply a complex-valued $B_1(\omega, p)$ for real p close to α_L^{-1}, because of $R_{\beta_L}(p)$. Zeros of $B_1(\omega, \alpha_L^{-1})$ may of course appear at complex ω, but the real and imaginary parts of $B_1(\omega, \alpha_L^{-1})$ will typically not vanish for the same real ω.

4.3. APPROACHING THE WAVENUMBER LIMIT q AS ω TENDS TO ZERO

The medium slownesses α^{-1} and β^{-1} will not depend on ω in the absorption-free case. As ω tends to zero, each modal wavenumber trajectory $k(\omega) = \omega p(\omega)$ will reach its limit q. It follows from equations (13) and (16) that terms of magnitude $\mathcal{O}(p^{-2})$, or $\mathcal{O}(\omega^2)$, are lost when the ODE systems (5) and (6) for the wavenumber limits q are derived. Hence, for $q \neq 0$, we may conclude that

$$k(\omega) \approx q + \gamma\omega^2 \tag{42}$$

for some γ as ω tends to zero. In particular, $\lim_{\omega \to 0} k'(\omega) = 0$.

4.4. INCLUDING ABSORPTION

When absorption is introduced into the medium, with complex medium slownesses, the double roots will in general disappear and the branch points will not be hit exactly. This is a consequence of the fact that the reduction to a real-valued function is lost. Trajectory identification may become easier, however. In fact, introduction of slight absorption is often useful to pair together path segments upon exit from a double root. The change of Riemann sheets close to a branch point will now be achieved by a path *around* the branch point, crossing the branch cut.

For a real slowness trajectory $p(\omega)$ on the physical Riemann sheet in the absorption-free case, it is natural to require the group slowness $\partial k/\partial\omega$ to be positive

(e.g., reference [10, section 1A]). This dictates the choice of a positive or negative $p(\omega)$. It follows from reference [19, (7.78)], and the fact that bulk and shear moduli are restricted to the fourth quadrant [26, section 9.5], that this choice is consistent with the requirement that $p(\omega)$ get a positive imaginary part when absorption is introduced.

5. AN EXAMPLE FROM PLATE ACOUSTICS

A solid–fluid–solid trilayer surrounded by air, with a 0·83 mm glass plate and a 0·61 mm aluminium plate separated by 0·55 mm water, was considered in reference [14]. The P- and S-velocity parameters of the glass were 5·568 and 3·402 km/s, and the glass density was 2·2 kg/dm^3. The corresponding parameters for the aluminium were 6·452 and 3·100 km/s, and 2·7 kg/dm^3, and the water velocity was 1·478 km/s. No absorption was introduced. A point made by the authors was that the dispersion curves of the trilayer could be analyzed in terms of the dispersion in the decoupled constituent layers. Considering quotients of acoustic impedances, they inferred that the glass and aluminium plates should be considered stress-free at their interfaces, while the water layer should be considered to be rigidly held.

The interface conditions proposed in reference [14] are obviously of the same type as those introduced in section 2.1. By turning to very low frequencies, below cutoff where the modal slowness leaves the real axis, which was not done in reference [14], we have seen that these interface conditions emerge regardless of the acoustic impedance values. Applying the techniques and results of sections 2 and 3, the low-frequency mode structure (for modes such that $\liminf_{\omega\to 0}|k(\omega)| < \infty$) can be specified as follows. For convenience, the surrounding air is replaced by vacuum.

There are 14 modes for which $\lim_{\omega\to 0} k(\omega) = 0$. We have two quasilongitudinal waves for each of the two solid layers [16, Theorem 4.1(i)], four bending waves of asymptotic type $\omega^{-1/2}$ for $p(\omega)$ [16, Theorem 6.1(ii)], and six bending waves of asymptotic type $\omega^{-2/3}$ for $p(\omega)$ [16, Theorem 6.1(iv)]. These 14 modes are depicted schematically in Figure 1.

The modes with non-zero wavenumber limits q are infinite in number, and the q values close to the origin are shown in Figure 2. Considering the modes to be "born" at low frequency, we get a classification according to glass-born, water-born, and Al-born modes. In this case, the q for glass- and Al-born modes are obtained from the simple equations $\sinh(qd) \pm qd = 0$ according to equation (1), and the different thicknesses of the glass and aluminium layers are directly reflected in Figure 2. (For non-homogeneous solid regions, including coating, for example, the compound-matrix computation techniques of section 3 would be needed). The limits q for the water-born modes appear as $q = n\pi\mathrm{i}/0{\cdot}55\ \mathrm{mm}^{-1}$, where n is a non-vanishing integer, according to section 2.1 and equation (24).

Usual dispersion curves for real p are drawn in Figure 3. Compared to the corresponding curves in reference [14, Fig. 10], there are a few differences. The vertical axis is for horizontal slowness in s/km rather than incidence angle in degrees, and it extends to 0·75 s/km in order to include the two slow modes with real $p(\omega)$ tending to infinity as ω tends to zero. These modes have been given the

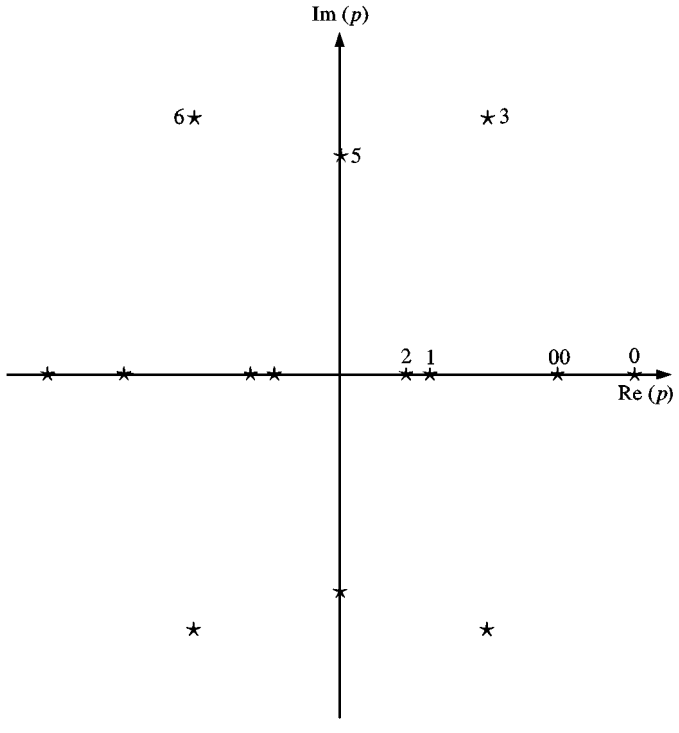

Figure 1. Configuration in principle of the 14 modal slownesses $p(\omega)$ with $\lim_{\omega\to 0} k(\omega) = 0$ for a solid–fluid–solid medium with free boundaries. There are six modes on an outer circle tending to infinity like $\omega^{-2/3}$, four modes on an inner circle tending to infinity like $\omega^{-1/2}$, and four modes with slownesses tending to real constants. The mode numbers give the connection to the dispersion curves in Figure 3.

numbers 0 and 00. Parts of the slowness trajectories for modes 10, 12, and 15 have been shifted to negative p to comply with the requirement of a positive group slowness (section 4.4).

By mode tracking in the complex plane, below cutoff and down to very low frequencies, we may connect the modes shown in Figure 3 to the low-frequency mode structure shown in Figures 1 and 2. The appropriate mode numbers from Figure 3 have actually been included already in Figures 1 and 2. The seven modes with vanishing low-frequency wavenumber limits (half of 14 modes, taking account of $+-$ symmetry) are modes 0, 00, 1, 2, 3, 5, and 6. Here, modes 1 and 2 are the quasilongitudinal modes, modes 00 and 5 are the bending waves of asymptotic type $\omega^{-1/2}$ for $p(\omega)$, and modes 0, 3, and 6 are the bending waves of asymptotic type $\omega^{-2/3}$ for $p(\omega)$. Among modes with $q \neq 0$, modes 8, 10, 14, 15 are glass-born, modes 4, 7, 9, 13, 16 are water-born, and modes 11, 12, 17 are Al-born. All modes in Figure 1 and all modes with small q in Figure 2 are indeed included, suggesting a one-to-one correspondence with the set of modes for which p becomes real as ω becomes large.

Figures 4 and 5 show some modal slowness trajectories, in schematic form, as determined by the mode tracking for decreasing ω. Mirror modes, for $\pm p$, are indicated by a minus sign and dotted trajectories. For clarity, the trajectories have been displaced from the axes even when $p(\omega)$ is real or imaginary. In particular, the

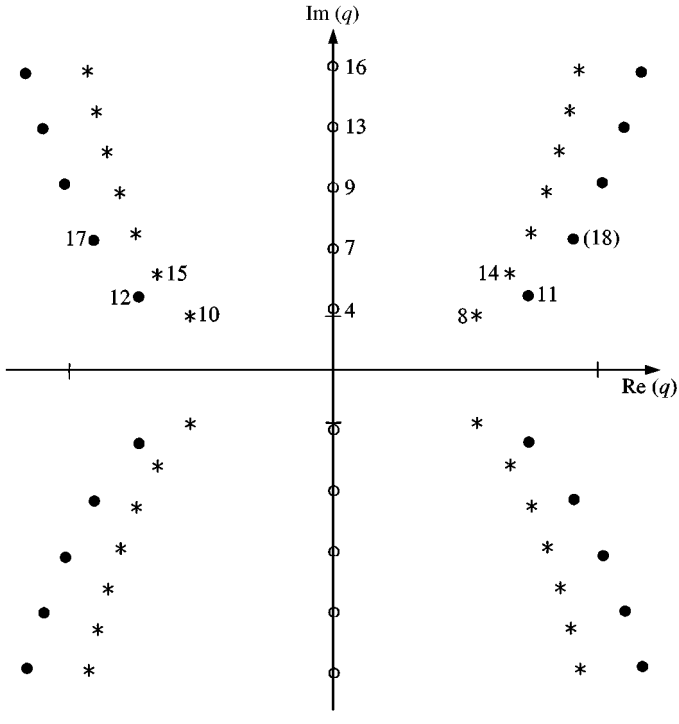

Figure 2. Non-vanishing low-frequency wavenumber limits for the solid–fluid–solid medium in section 5. Glass-, water-, and Al-born modes are denoted by the symbols *, ○, and ● respectively. The mode numbers give the connection to the dispersion curves in Figure 3. The bars on the axes denote $\pm 5\ \mathrm{mm}^{-1}$. Note the significantly different scales for the real and imaginary parts.

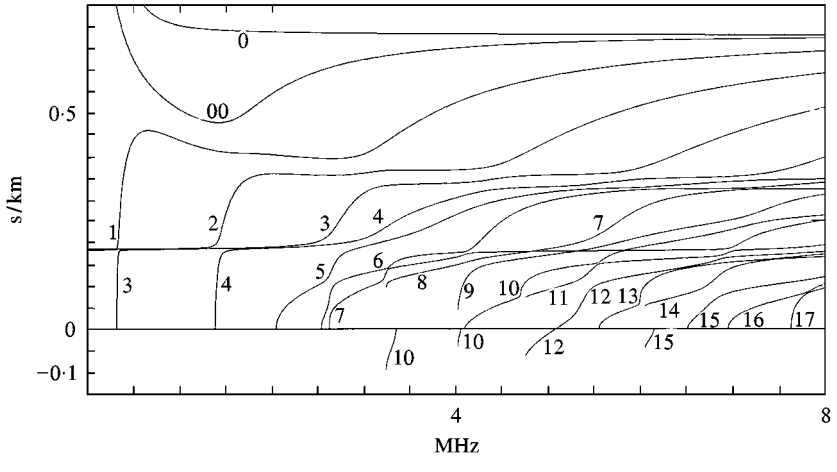

Figure 3. Dispersion curves for the solid–fluid–solid medium discussed in section 5.

horizontal and vertical line segments close to the axes are actually on the real and imaginary axes, respectively. The upper panel of Figure 4 shows the typical trajectory for a fluid-born mode, with a double root at the origin formed by the mode and its mirror mode (section 4.1).

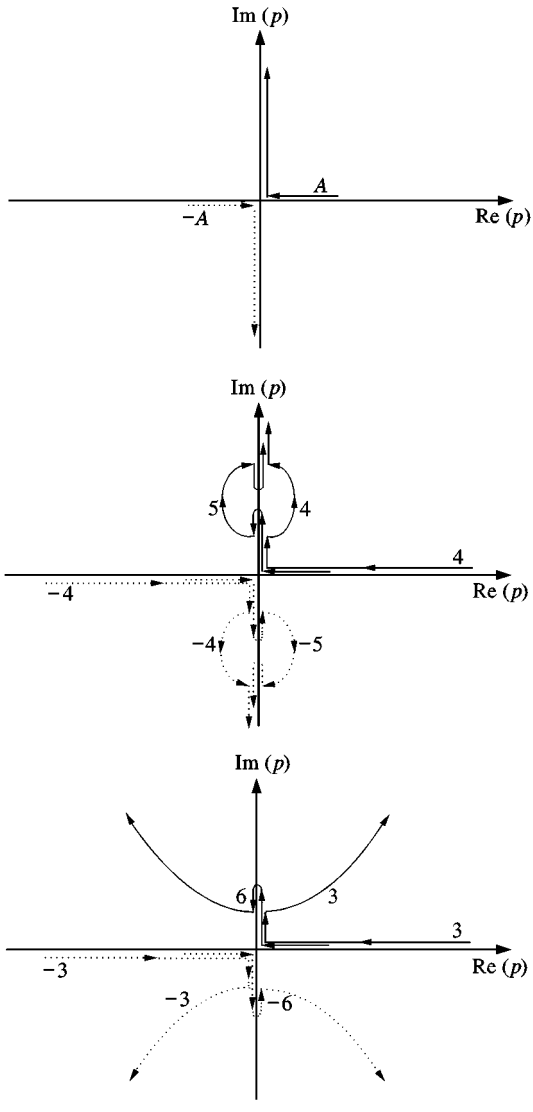

Figure 4. Trajectories for $p(\omega)$, in principle, as ω decreases for the solid–fluid–solid medium. Upper panel: A is for modes 7, 13, 16. Middle and lower panels: the mode numbers have been indicated.

The middle panel of Figure 4 concerns modes 5 and 4, with two double roots at the origin (one for modes 5 and -5, and one for modes 4 and -4) and two double roots on the positive imaginary axis (both involving modes 5 and 4). For low frequencies, the $p(\omega)$ for modes 4 and 5 proceed with different speeds towards infinity along the positive imaginary axis, in such a way that $k(\omega)$ for mode 4 tends to an imaginary number whereas $k(\omega)$ for mode 5 tends to zero ($\omega^{1/2}p(\omega)$ for mode 5 tends to an imaginary number).

The two modes 6 and 3, of asymptotic type $\omega^{-2/3}$ for $p(\omega)$ and with complex low-frequency limits for $\omega^{2/3}p(\omega)$, appear in the lower panel of Figure 4. There are

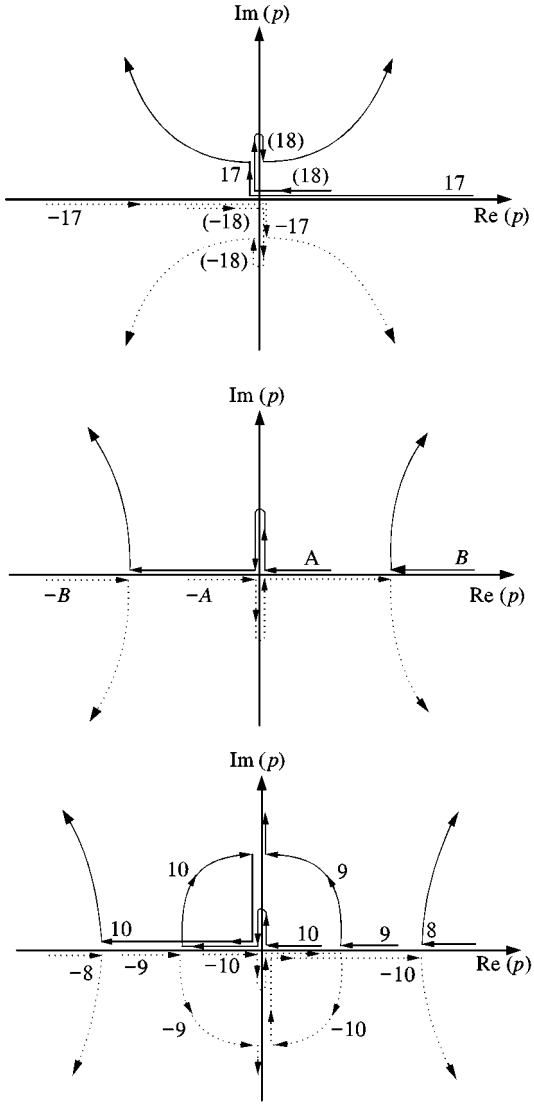

Figure 5. Trajectories for $p(\omega)$, in principle, as ω decreases for the solid–fluid–solid medium. Middle panel: modes (A, B) are modes (12, 11), (15, 14). Upper and lower panels: the mode numbers have been indicated. Concerning the lower panel, there is a tiny additional feature which has not been included. Mode 10 actually turns back and forth once on its way down the imaginary axis after colliding with mode 9. (Of course, the mirror mode -10 exhibits the analogous behaviour).

two double roots at the origin (one for modes 6 and -6, and one for modes 3 and -3) and one double root on the positive imaginary axis.

It was noted in section 4.1 that solid-born modes have to combine by forming a double root on the axes in order to produce quartets of low-frequency modal slownesses in the complex plane. The upper panel of Figure 5 concerns modes 18 (just outside the scope of Figure 3) and 17, joining at a double root on the imaginary axis, while the middle panel concerns modes joining at double roots on

the real axis. In the latter case, one of the modes proceeds initially to the negative real axis (via a semiloop along the positive imaginary axis and two double roots at the origin together with its mirror mode).

The lower panel of Figure 5 illustrates what may happen when a fluid-born mode (9) appears between two solid-born modes (10 and 8). With a typical trajectory according to the upper panel of Figure 4, mode 9 would disturb a combination of modes 10 and 8 according to the middle panel of Figure 5. To handle this problem, mode 9 is moved out into the complex plane after forming a double root on the positive real axis together with mode -10. Subsequently, mode 10 initializes a loop in the second quadrant. It forms a double root with mode 9 on the positive imaginary axis. Mode 9 is thereby brought back to the axes, and it may proceed towards its imaginary wavenumber limit as ω tends to zero. At the same time, mode 10 can complete its loop by forming a double root with its mirror mode at the origin and proceeding along the negative real axis towards its collision point with mode -8.

It is also useful to consider the evolution of the mode shapes as ω tends to zero. Figure 6 provides illuminating "waterfall plots" for glass-born mode 8, water-born mode 9, and Al-born mode 11. It is below cutoff that the mode shapes become simple (the cut-off frequencies can be read from Figure 3). Figure 6 concerns normal traction, and the effective free interface conditions for the solid-born modes appear quite clearly. Modes 8 and 11 are apparently the lowest-order glass-born and Al-born modes, respectively. Mode 9 is the third-order water-born mode (after modes 4 and 7). This can also be clearly seen, although a plot of vertical displacement would be preferable for illustrating the water-born modes and their effective boundary conditions of rigid type. The mode shapes shown are in perfect agreement with the theoretical results in reference [17, Theorem 5.2].

6. AN EXAMPLE FROM UNDERWATER ACOUSTICS

As a fluid–solid medium example from underwater acoustics, let us consider a shallow-water waveguide with a homogeneous 50 m deep water layer with velocity 1·430 km/s overlying a solid sediment bottom. The surface is assumed to be free (pressure-release). The sediment bottom consists of two 10 m thick layers, an upper sand/clay layer with P-velocity 1·700 km/s, S-velocity 0·650 km/s, and density 1·5 kg/dm^3, and a lower till layer with P-velocity 2·000 km/s, S-velocity 1·000 km/s, and density 1·9 kg/dm^3. Below these two sediment layers, there is a homogeneous crystalline bedrock half-space with P-velocity 6·000 km/s, S-velocity 4·000 km/s, and density 2·6 kg/dm^3. The parameter values have been chosen with a view to representative conditions for parts of the Baltic. However, the half-space velocities are somewhat high since we wish to have the S-wave branch point at a convenient point (0·25 s/km) for visual purposes. In addition, absorption has not been included in order to keep the high-frequency parts of the dispersion curves real-valued.

Applying the techniques and results of sections 2 and 3, the low-frequency mode structure (for modes such that $\liminf_{\omega\to 0}|k(\omega)| < \infty$) can be specified as follows. Since the lower termination of the medium is a homogeneous solid half-space, we

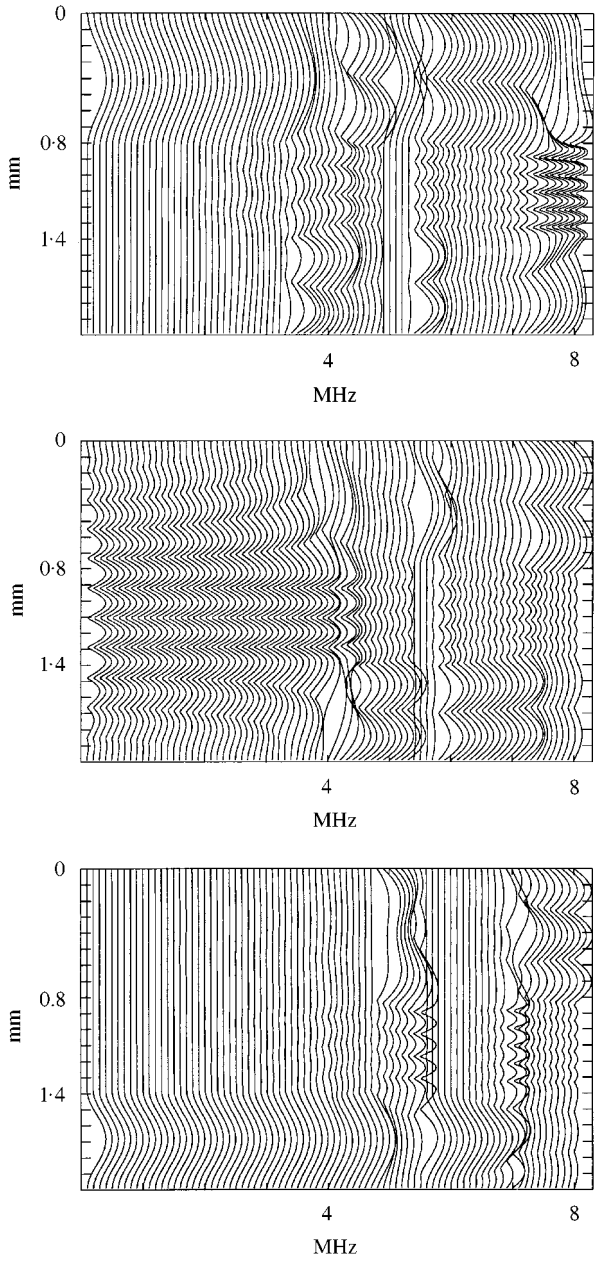

Figure 6. "Waterfall plots" showing depth dependence of modal normal traction magnitude from 0·1 to 8 MHz. The medium is the solid–fluid–solid trilayer considered in section 5, with water between 0·83 and 1·38 mm. The vertical axes are for depth, from 0 mm down to 2 mm. Upper panel: glass-born mode 8, middle panel: water-born mode 9, lower panel: Al-born mode 11.

have to deal with four Riemann sheets, $++$, $-+$, $+-$, and $--$, as defined in section 4.2.

There are 12 modes for which $\lim_{\omega\to 0} k(\omega) = 0$. They are all of Rayleigh type [16, Theorem 4.1(iii)]. There are four modes on the $+-$ sheet for small ω, and we

denote them by 1, 2, $\bar{1}$, and $\bar{2}$. As ω tends to zero, mode 1 approaches $p = 0{\cdot}112345$ s/km from the first quadrant, whereas mode 2 approaches $p = 0{\cdot}166650$ s/km, also from the first quadrant. Modes $\bar{1}$ and $\bar{2}$, with the bar suggesting the complex conjugate, exhibit the corresponding complex conjugate slownesses for small ω. These four modes become leaky Rayleigh waves, which have real phase velocities for a sufficiently small Poisson ratio [26, section 3.4].

We know from section 4.2 that the sign-shifted modal slownesses appear on the "opposite" Riemann sheet. Accordingly, we denote the corresponding modes on the $-+$ sheet by -1, -2, $-\bar{1}$, and $-\bar{2}$.

On each of the $++$ and $--$ sheets, there is a wave with p tending to the ordinary Rayleigh slowness 0·279922 s/km as the frequency tends to zero. We denote these modes by 0, on each of the two sheets. In each case, the mode -0 appears in addition on the "opposite" sheet. All 12 modes with $\lim_{\omega \to 0} k(\omega) = 0$ have thereby been accounted for.

The modes with non-zero wavenumber limits q are infinite in number, and the q values close to the origin are shown in Figure 7. Considering the modes to be "born" at low frequency, we get a classification according to fluid- and solid-born modes. The computation of the q for the solid-born modes was done using the winding-number integral technique of reference [20], combined with factorization of the compound-matrix propagators as proposed in section 3.1. The limits q for the fluid-born modes appear simply as $q = (n + 1/2)\pi \mathrm{i}/0{\cdot}050\ \mathrm{km}^{-1}$, where n is an integer, as obtained from section 2.1 and equation (24). According to equation (8), the same non-zero q will appear on the $+-$ and $-+$ sheets. It follows from the rules in section 4.2 that the off-axes solid-born modal q in the upper panel of Figure 7 must appear in quartets, in a "$q, -q, \bar{q}, -\bar{q}$" pattern, and that the wavenumber limits for modes 3, 6, -7, 11 there are purely imaginary. As concerns the lower panel, there is only a "$q, \bar{q}$" pattern. For example, the wavenumber limits for modes 7 and 8 there are $q = 154{\cdot}449 + 270{\cdot}809\mathrm{i}\ \mathrm{km}^{-1}$ and $q = -149{\cdot}011 + 271{\cdot}407\mathrm{i}\ \mathrm{km}^{-1}$, respectively. The q on the $++$ sheet are not shown in Figure 7, but they are obtained from the q of the $--$ sheet by changing signs.

Usual dispersion curves for real p are drawn in Figure 8. Note that the $++$ and $+-$ sheets have been combined in the upper panel, and that the $-+$ and $--$ sheets have been combined in the lower panel. The horizontal slowness p increases upwards for the $++$ and $-+$ sheets, and it increases downwards for the $+-$ and $--$ sheets. The central horizontal line in each panel is for the S-wave branch point slowness 0·25 s/km. This kind of diagram combination is quite appropriate in view of the results presented in section 4.2 concerning passage of the branch point with the largest slowness. Indeed, except for one of the lowest-order modes 0, each mode from the $++$ and $-+$ sheets in Figure 8 will hit the S-wave branch point as the frequency is decreased and change Riemann sheets. This behaviour is particularly clear in the figure concerning the modes from the $-+$ sheet and mode 3 from the $++$ sheet. Most of the modes from the $++$ sheet will leave the real axis on the $+-$ sheet and get complex horizontal slownesses very soon as the frequency is further decreased.

The mode numbers indicated in Figure 8 have been introduced separately for the upper and lower panels. Except for the lowest-order modes 0, the modal slownesses

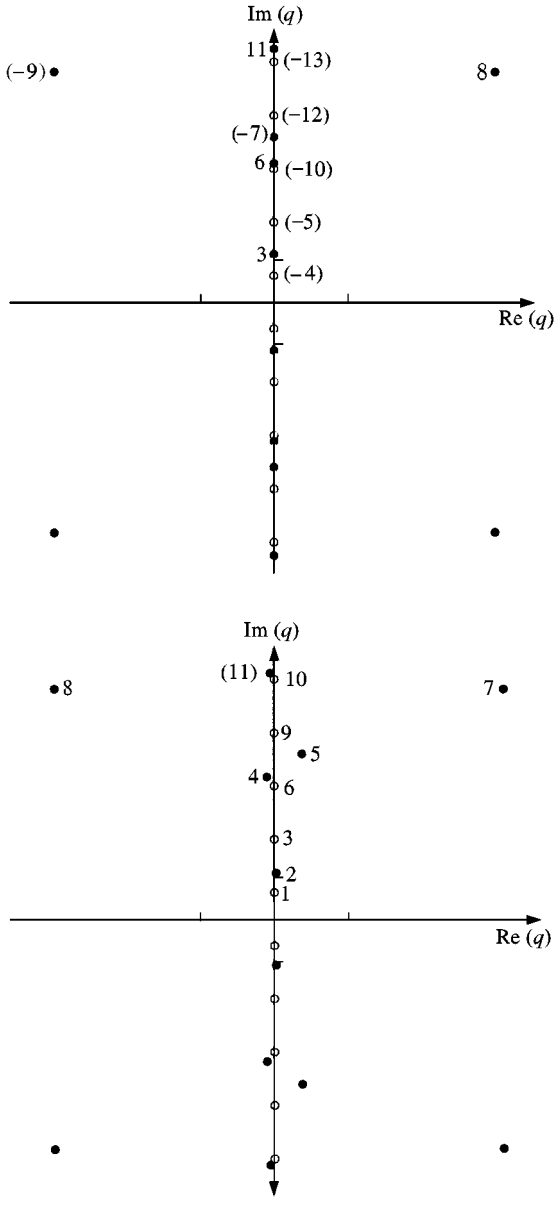

Figure 7. Non-vanishing low-frequency wavenumber limits on the $+-$ sheet (upper panel) and the $--$ sheet (lower panel) for the fluid–solid medium considered in section 6. Fluid- and solid-born modes are denoted by the symbols ○ and ●, respectively. The mode numbers in the two panels give the connection to the dispersion curves on the $++$ and $-+$ sheets, respectively, in Figure 8. The bars on the axes denote $\pm 50\,\mathrm{km}^{-1}$. Note the different scales for the real and imaginary parts.

combine in pairs at double roots to form conjugate complex numbers (not shown) as the frequency is decreased. The notation with "1, $\bar{1}$", etc., has been used in the obvious way to indicate this grouping of modes. Note that mode 0 from the $-+$ sheet proceeds with a real slowness on the $--$ sheet after hitting the S-wave branch point. It approaches the ordinary Rayleigh slowness as the frequency tends to zero.

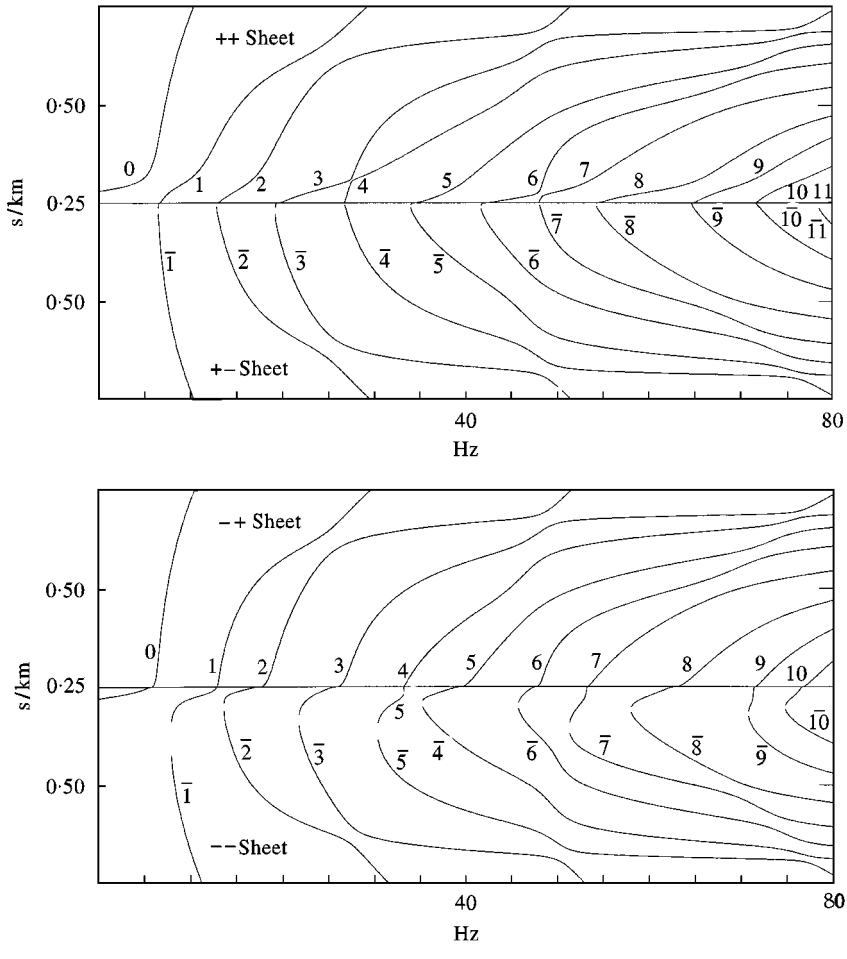

Figure 8. Dispersion curves for the fluid–solid medium considered in section 6.

By mode tracking in the complex plane, down to very low frequencies, we may connect the modes shown in Figure 8 to the low-frequency mode structure as specified for the $q = 0$ modes and shown in Figure 7 for the $q \neq 0$ modes. The appropriate mode numbers from Figure 8 have already been included in Figure 7. Restricting ourselves to the modes with non-zero low-frequency wavenumber limits q, it turns out that the modes from the $++$ and $+-$ sheets in Figure 8 will appear on the $+-$ or $-+$ sheets when the frequency has become low enough, and that the modes from the $-+$ and $--$ sheets in Figure 8 will appear on the $--$ sheet at low frequency.

The six modes with vanishing low-frequency wavenumber limits (half of 12 modes, taking account of $+-$ symmetry) are modes 0, 1, 2, $\bar{1}$, and $\bar{2}$ from the $++$ and $+-$ sheets, and mode 0 from the $-+$ and $--$ sheets. Among modes with $q \neq 0$, modes 4, 5, 10 (and $\bar{4}$, $\bar{5}$, $\bar{10}$) from the $++$ and $+-$ sheets are fluid-born, as are modes 1, 3, 6, 9, 10 (and $\bar{1}$, $\bar{3}$, $\bar{6}$, $\bar{9}$, $\bar{10}$) from the $-+$ and $--$ sheets. The

remaining modes 3, 6, 7, 8, 9, 11 (and $\bar{3}$, $\bar{6}$, $\bar{7}$, $\bar{8}$, $\bar{9}$, $\bar{11}$) from the $++$ and $+-$ sheets are solid-born, as are the remaining modes 2, 4, 5, 7, 8 (and $\bar{2}$, $\bar{4}$, $\bar{5}$, $\bar{7}$, $\bar{8}$) from the $-+$ and $--$ sheets.

All modes with vanishing low-frequency wavenumber limits and all modes with small q in Figure 7 are indeed included, suggesting a one-to-one correspondence with the set of modes for which p becomes real as ω becomes large.

Figure 9 shows some modal slowness trajectories, in schematic form, as determined by the mode tracking for decreasing ω. As in Figures 4 and 5, the trajectories have been displaced from the axes even when $p(\omega)$ is real or imaginary. The upper and middle panels of Figure 9 show typical trajectories as the frequency is decreased, with a change of Riemann sheets at the S-wave branch point (indicated by the rightmost vertical bar) and a subsequent escape into the complex plane initiated by a collision at a double root. In the middle panel, a further change of Riemann sheets, from $+-$ to $-+$, takes place as the trajectory crosses the branch cuts to the left of the P-wave branch point (the left vertical bar on the positive real axis). The trajectories for modes A and $\bar{\text{A}}$ intersect at the same frequency here, but by temporarily changing to branch cuts that do not interfere, the "apparent" intersection involves different Riemann sheets and there is no double root for $D(\omega, p)$.

The lower panel of Figure 9 illustrates the complicated trajectories formed by modes, 4, 5, $\bar{4}$, and $\bar{5}$ from $-+$ and $--$ sheets in Figure 8. As the frequency is decreased, mode 5 hits the S-wave branch point and moves to the $--$ sheet where it collides with mode $\bar{4}$. The two modes move out into the complex plane, but they return to the real axis at another double root at a smaller p. By lowering the frequency further, mode 5 can proceed out along the positive real slowness axis and enter the complex plane by forming a double root together with mode $\bar{5}$. Mode $\bar{4}$ can proceed to smaller real p and meet mode 4, which is on its way out along the positive real axis after having hit the S-wave branch point and changed Riemann sheets.

In effect, mode 5 forms a loop causing modes $\bar{4}$ and $\bar{5}$ to change places in the lower panel of Figure 8. Similar complications are not uncommon when tracking dispersion curves. For example, we may compare with the plait patterns regularly observed in dispersion curves for free homogeneous solid plates, e.g., reference [9].

The double roots referred to appear on the $+-$ or $--$ sheets. They are not on the physical sheet, and it is not obvious how the trajectories will be changed when absorption is introduced. In fact, it turns out that the behaviour will be different if absorption is introduced in the homogeneous solid half-space or in the sediment layers. The trajectories depicted schematically in Figure 9 are in agreement with the effect of slight absorption in the homogeneous half-space but no absorption in the sediment layers. The mode-number connections for the wavenumber limits in Figure 7 have also been adapted to this case, as concerns "q or $\bar{q}$".

As in section 5, it is useful to consider the evolution of the mode shapes as ω tends to zero. Figure 10 provides illuminating "waterfall plots" for some modes from the $++$ and $+-$ sheets in Figure 8: the fluid-born modes 4 and 5, and the solid-born modes 3 and 6. Again, it is below cutoff that the mode shapes become simple. The cut-off frequencies where the Riemann sheet is changed at the S-wave branch point,

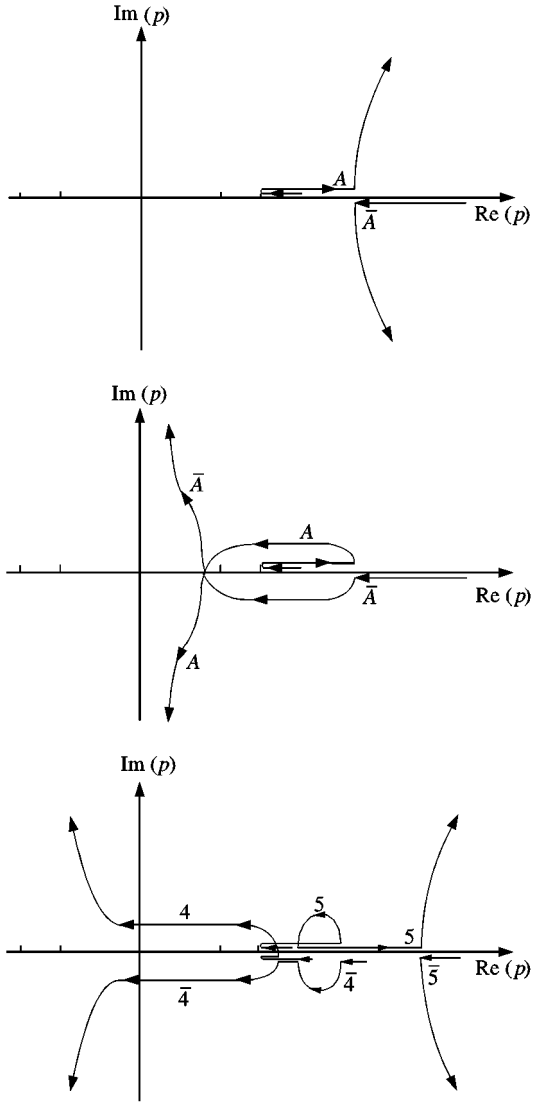

Figure 9. Trajectories for $p(\omega)$, in principle, as ω decreases for the fluid–solid medium. Upper panel: at high frequency, A is for modes 3, 6, 8, 11 on the $++$ sheet and modes 1, 2, 3, 6, 7, 8, 9, 10 on the $-+$ sheet. Additional features may appear. For example, the trajectory for the former mode 6 has a small loop in the first quadrant. Although this has not been indicated, the low-frequency limits may appear at different sides of the imaginary axis (cf. the actual wavenumber limits according to Figure 7). Middle panel: at high frequency, A is for modes 4, 5, 7, 9, 10 on the $++$ sheet. Lower panel: the mode numbers have been indicated, at high frequency these modes are on the $-+$ and $--$ sheets.

and the lower frequencies where $p(\omega)$ becomes complex at a double root, can be read from Figure 8. Above cutoff, the dispersion curves exhibit a terrace-like structure (cf. Figure 8) that is interrupted by osculation points at which modal properties are exchanged and repulsion phenomena appear (cf. reference [27]).

Figure 10 concerns normal traction, and the effective free interface conditions for the solid-born modes 3 and 6 appear quite clearly. Modes 4 and 5 are the

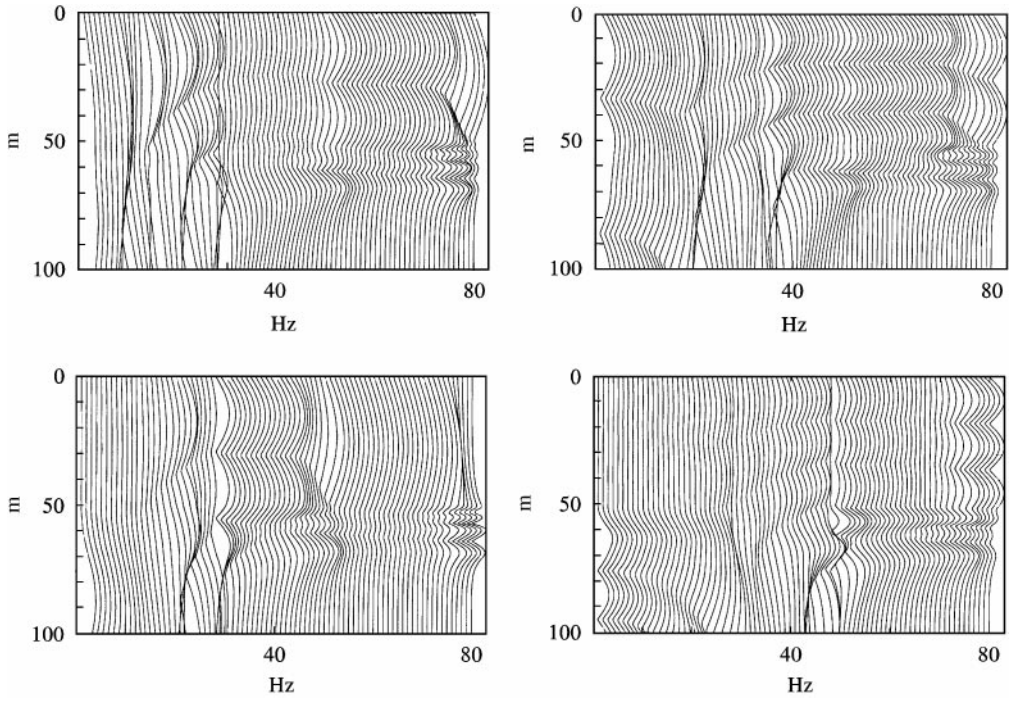

Figure 10. "Waterfall plots" showing depth dependence of modal normal traction magnitude from 1 to 80 Hz. The medium is the fluid–solid medium considered in section 6, with fluid between 0 and 50 m. The vertical axes are for depth, from 0 m down to 100 m. Upper panels: fluid-born modes 4 (left) and 5 (right), lower panels: solid-born modes 3 (left) and 6 (right). All four modes are on the $++$ sheet at the higher frequencies according to Figure 8, but they become leaky after hitting the S-wave branch point.

lowest-order and second-lowest-order fluid-born modes, respectively. The mode shapes shown are in perfect agreement with the theoretical results in reference [17, Theorem 5.2].

7. DISCUSSION

We have seen that the low-frequency mode structure, comprising all modes for which $\liminf_{\omega\to 0}|k(\omega)| < \infty$, can be determined for each fluid–solid medium. The wavenumber limit $q = \lim_{\omega\to 0} k(\omega)$ always exists for such a mode. There will be a finite number of modes with $q = 0$ [16; 17, Appendix A]. The modes with $q \neq 0$ decouple into region-dependent classes, each fluid and each solid region in the medium provides modes with low-frequency wavenumber limits q according to the zeros of a certain entire analytic function. In the presence of homogeneous half-spaces, different analytic functions may appear for the different Riemann sheets. Effective low-frequency boundary conditions develop at the fluid–solid interfaces, with "rigid" towards the fluid and "free" towards the solid.

The low-frequency mode structure can be carried to higher frequencies by tracking dispersion curves, i.e., by following continuous modal slowness trajectories

$p(\omega)$ for varying ω. In the ideal case, each trajectory $p(\omega)$ will extend continuously from arbitrarily small ω to arbitrarily large ω, covering the whole interval $(0, \infty)$, and there are no modes with $\lim_{\omega\to 0}|k(\omega)| = \infty$. Furthermore, for an absorption-free medium, it appears that each $p(\omega)$ will typically approach the real axis and it may ultimately become real as ω tends to infinity. Under these ideal circumstances, the rigorously derived low-frequency mode structure imposes a canonical mode structure at each ω, with a perfect one-to-one connection to ordinary real-valued dispersion curves as ω becomes large. Indeed, our examples in sections 5 and 6 appear to be of this satisfactory type.

Unfortunately, there are exceptions to the ideal behaviour just outlined. First, there are media which support low-frequency modes for which $\lim_{\omega\to 0}|k(\omega)| = \infty$. The simplest example appears to be a Pekeris waveguide, a homogeneous fluid layer with P-velocity α and density ρ between a free or rigid surface and a lower homogeneous fluid half-space with P-velocity α_L and density ρ_L, for which the density is constant ($\rho = \rho_L$). The asymptotic behaviour of the modes, with $\lim_{\omega\to 0}|k(\omega)| = \infty$, was specified in reference [16, (7.1)]. The upper termination of the medium may alternatively be another homogeneous half-space, either fluid or solid, for which the density ρ_U may be arbitrary. All of these modes with $\lim_{\omega\to 0}|k(\omega)| = \infty$ are leaky for small ω, with an exponential increase or inward direction of oscillation in a terminating homogeneous half-space. We are not aware of non-leaky examples. For homogeneous fluid or solid plates with free or rigid boundaries, the low-frequency modal wavenumber limits do always exist as finite complex numbers.

A second imperfection is that we are not certain that each trajectory $p(\omega)$ can always be defined on all of $(0, \infty)$. To illustrate the potential problem, consider a simple medium with two homogeneous solid half-spaces separated by a fluid region with vanishing thickness. (We temporarily allow interior fluid regions with vanishing thickness.) The dispersion function can be expressed as

$$D(\omega, p) = \rho_L\beta_L^4\mathscr{R}_L(p)R_{\alpha_U}(p) + \rho_U\beta_U^4\mathscr{R}_U(p)R_{\alpha_L}(p), \tag{43}$$

where $R_\alpha(p) = (p^2 - \alpha^{-2})^{1/2}$ and $\mathscr{R}_L, \mathscr{R}_U$ are the Rayleigh functions [16, (2.21)]. Considering the leaky Riemann sheet defined for large p by $R_{\alpha_L}(p) \approx p$ and $R_{\alpha_U}(p) \approx -p$, it follows that

$$D(\omega, p) \approx \gamma_5 p^5 + \gamma_3 p^3 + \gamma_1 p + \gamma_{-1}p^{-1} + \cdots, \tag{44}$$

where $\gamma_5 = 8(\rho_U\beta_U^4 - \rho_L\beta_L^4)$ and γ_3 is typically non-vanishing. Let us now assume that β_U and β_L are frequency-dependent in such a way that $\gamma_5 = 0$ for $\omega = \omega_\infty > 0$ but that $\gamma_5 \neq 0$ for $\omega \neq \omega_\infty$. (Causality arguments prescribe some absorption in the half-spaces in this case.) It follows that there are trajectories $p(\omega)$ exhibiting a singularity ($p(\omega) \to \infty$) as ω tends to ω_∞.

A third appeal for caution concerns the anticipated connection to real-valued dispersion curves for high frequencies in the absorption-free case. True, there are mechanisms which appear to favour real $p(\omega)$ as p becomes large. Suppose for

simplicity that the largest medium slowness, c^{-1} say, appears within a layer of finite extent d in depth. For real p slightly less than c^{-1}, the dispersion function $D(\omega, p)$ will then be real even in the presence of homogeneous half-spaces. As ω tends to infinity, a countable infinity of real modal slownesses $p(\omega)$ will appear that increase towards c^{-1}, as controlled by the relative contribution of terms including the rapidly oscillating factors $\cos(\omega d(c^{-2} - p^2)^{1/2})$ and $\sin(\omega d(c^{-2} - p^2)^{1/2})$. Indeed, for a homogeneous solid plate with free boundaries, each $p(\omega)$ tends to $\pm\beta^{-1}$ as ω tends to infinity, if we disregard the lowest-order modes, for which $\pm p(\omega)$ tends to the ordinary Rayleigh slowness [9, p. 210; 28, p. 450]. Interface-wave slowness limits as ω tends to infinity may appear regularly, since the layers become thick as compared to wavelength when the frequency is increased.

However, there are simple examples for which the modal slowness $p(\omega)$ stays complex as ω tends to infinity. For a homogeneous solid half-space with a large Poisson ratio and a free boundary, there will be two conjugate complex leaky Rayleigh-mode slownesses $p(\omega)$ which are independent of ω [26, section 3.4]. Leaky modes that remain complex for high frequencies may also be quite common for media with low-velocity half-spaces. Such media are of interest in connection with studies of fluid-loaded plates, e.g., reference [12].

We do not know the precise existence conditions for modes with $\lim_{\omega\to 0}|k(\omega)| = \infty$, interrupted trajectories, or non-real high-frequency $p(\omega)$ in the absorption-free case. To clarify these issues would be topics for further research.

Dispersion curves as shown in general are typically restricted to the physical sheet and real phase velocities. There are of course good reasons for this restriction, since it is the modes above cutoff (and the "fundamental" modes without cutoff) that dominate the field in connection with long-range propagation. However, the mode structure above cutoff can be complicated since the modes may change character and exchange properties at osculation points. Interference with double roots and branch points cause further complications as concerns tracking of dispersion curves through cutoff. Nevertheless, we have seen that it is at very low frequencies, below cutoff, where the modal slowness no longer appears on the real axis of the physical sheet, that a simple mode structure evolves providing useful insight.

REFERENCES

1. M. Redwood 1960 *Mechanical Waveguides*. London: Pergamon Press.
2. F. Jensen, W. Kuperman, M. Porter and H. Schmidt 1994 *Computational Ocean Acoustics*. New York: AIP Press.
3. R. D. Mindlin 1957 *Proceedings of the* 11*th Annual Symposium on Frequency Control, U.S. Army Signal Engineering Laboratories, Fort Monmouth, NJ*, 1–40. Mathematical theory of vibrations of elastic plates.
4. R. D. Mindlin and M. A. Medick 1959 *Journal of Applied Mechanics* **26**, 561–569. Extensional vibrations in elastic plates.
5. R. D. Mindlin 1960 *First Symposium on Naval Structural Mechanics*, 1958 (J. N. Goodier and N. J. Hoff, editors), 199–232. Oxford: Pergamon Press. Waves and vibrations in isotropic, elastic plates.
6. J. W. C. Sherwood 1958 *Journal of the Acoustical Society of America* **30**, 979–984. Propagation in an infinite elastic plate.

7. J. D. Achenbach 1973 *Wave Propagation in Elastic Solids*. Amsterdam: North-Holland.
8. Y. H. Pao and R. K. Kaul 1974 *R. D. Mindlin and Applied Mechanics* (G. Herrmann, editor), 149–194. Oxford: Pergamon Press. Waves and vibrations in isotropic and anisotropic plates.
9. A. Freedman 1990 *Journal of Sound and Vibration* **137**, 209–230. The variation, with the Poisson ratio, of Lamb modes in a free plate, I: general spectra.
10. S. I. Rokhlin, D. E. Chimenti and A. H. Nayfeh 1989 *Journal of the Acoustical Society of America* **85**, 1074–1080. On the topology of the complex wave spectrum in a fluid-coupled elastic layer.
11. A. Freedman 1996 *Journal of the Acoustical Society of America* **99**, 3488–3496. Effects of fluid-loading on Lamb mode spectra.
12. X. L. Bao, H. Franklin, P. K. Raju, H. Uberall and O. Poncelet 1998 *Acustica* **84**, 823–829. Fluid-borne and Lamb-type waves on elastic plates in contact with two different fluids.
13. D. G. Crighton 1979 *Journal of Sound and Vibration* **63**, 225–235. The free and forced waves on a fluid-loaded elastic plate.
14. J. Laperre and W. Thys 1994 *Journal of the Acoustical Society of America* **96**, 1643–1650. Mode coupling in solid/liquid/solid trilayers.
15. F. Coulouvrat, M. Rousseau, O. Lenoir and J.-L. Izbicki 1998 *Acustica* **84**, 12–20. Lamb-type waves in a symmetric solid–fluid–solid trilayer.
16. S. Ivansson 1998 *SIAM Journal of Applied Mathematics* **58**, 1462–1508. A class of low-frequency modes in laterally homogeneous fluid–solid media.
17. S. Ivansson 1999 Low-frequency wavenumber limits for P-SV modes (submitted).
18. S. Ivansson 1997 *Zeitschrift fur Angewandte Mathematic und Mechanic* **77**, 767–776. The compound matrix method for multi-point boundary-value problems.
19. K. Aki and P. Richards 1980 *Quantitative Seismology*. San Francisco: Freeman.
20. S. Ivansson and I. Karasalo 1993 *Journal of Sound and Vibration* **161**, 173–180. Computation of modal wavenumbers using an adaptive winding-number integral method with error control.
21. S. Ivansson 1999 *Journal of the Acoustical Society of America* **106**, 61–72. Low-frequency slow-wave dispersion computations by compound-matrix propagation.
22. S. Ivansson 1993 *Journal of Computational Physics* **108**, 357–367. Delta-matrix factorization for fast propagation through solid layers in a fluid–solid medium.
23. S. Ivansson 1998 *Geophysical Journal International* **132**, 725–727. Comment on 'Free-mode surface-wave computations' by P. Buchen and R. Ben-Hador.
24. S. Ivansson 1998 *Zeitschrift fur Angewandte Mathematic und Mechanic* **78**, 231–242. The compound matrix method for multi-point boundary-value problems depending on a parameter.
25. S. Ivansson and I. Karasalo 1998 *Proceedings of the 4th European Conference on Underwater Acoustics* (A. Alippi and G. B. Cannelli, editors), 685–690. Rome: CNR-IDAC. Double-root resonances and complex modal slownesses in a fluid–solid medium.
26. J. A . Hudson 1980 *The Excitation and Propagation of Elastic Waves*. Cambridge: Cambridge University Press.
27. H. Uberall, B. Hosten, M. Deschamps and A. Gerard 1994 *Journal of the Acoustical Society of America* **96**, 908–917. Repulsion of phase-velocity dispersion curves and the nature of plate vibrations.
28. K. F. Graff 1975 *Wave Motion in Elastic Solids*. Belfast: Ohio State University Press.

APPENDIX A: CANCELLATION-FREE LOW-FREQUENCY PROPAGATORS FOR HOMOGENEOUS LAYERS

It was shown in reference [21] that problems with loss of numerical precision by cancellation effects may be encountered in connection with slow-wave dispersion

computations at very low frequencies. The problems arise from the usual expressions for the individual elements of the propagator matrices for homogeneous solid layers. Alternative cancellation-free expressions had to be derived in reference [21] to ascertain adequate accuracy.

The modes considered in reference [21] were slow modes for which the horizontal slowness p tends to infinity while the horizontal wavenumber $k = \omega p$ tends to zero as ω tends to zero. It turns out that the numerical cancellation problems and the cure are quite analogous for *all* modes for which p tends to infinity while k tends to a finite complex number q as ω tends to zero.

Assuming a fixed $q \neq 0$, we rewrite equations (21)–(23) as

$$\mathbf{P}_F(\omega, p) \approx \mathrm{diag}(1, p^{-1}) \cdot \mathbf{Q}_F(q) \cdot \mathrm{diag}(1, p), \tag{A1}$$

$$\mathbf{P}_S(\omega, p) \approx \mathrm{diag}(p^{-1}, p^{-1}, 1, 1) \cdot \mathbf{Q}_S(q) \cdot \mathrm{diag}(p, p, 1, 1), \tag{A2}$$

$$\mathbf{P}_S^{A_2}(\omega, p) \approx \mathrm{diag}(p^{-1}, 1, 1, 1, 1, p) \cdot \mathbf{Q}_S^{A_2}(q) \cdot \mathrm{diag}(p, 1, 1, 1, 1, p^{-1}) \tag{A3}$$

for small ω with $p = q/\omega$. It follows that

$$\mathbf{P}_F(\omega, p) = \begin{pmatrix} \mathcal{O}(1) & \mathcal{O}(p) \\ \mathcal{O}(p^{-1}) & \mathcal{O}(1) \end{pmatrix}, \tag{A4}$$

$$\mathbf{P}_S(\omega, p) = \begin{pmatrix} \mathcal{O}(1) & \mathcal{O}(1) & \mathcal{O}(p^{-1}) & \mathcal{O}(p^{-1}) \\ \mathcal{O}(1) & \mathcal{O}(1) & \mathcal{O}(p^{-1}) & \mathcal{O}(p^{-1}) \\ \mathcal{O}(p) & \mathcal{O}(p) & \mathcal{O}(1) & \mathcal{O}(1) \\ \mathcal{O}(p) & \mathcal{O}(p) & \mathcal{O}(1) & \mathcal{O}(1) \end{pmatrix}, \tag{A5}$$

$$\mathbf{P}_S(\omega, p)^{A_2} = \begin{pmatrix} \mathcal{O}(1) & \mathcal{O}(p^{-1}) & \mathcal{O}(p^{-1}) & \mathcal{O}(p^{-1}) & \mathcal{O}(p^{-1}) & \mathcal{O}(p^{-2}) \\ \mathcal{O}(p) & \mathcal{O}(1) & \mathcal{O}(1) & \mathcal{O}(1) & \mathcal{O}(1) & \mathcal{O}(p^{-1}) \\ \mathcal{O}(p) & \mathcal{O}(1) & \mathcal{O}(1) & \mathcal{O}(1) & \mathcal{O}(1) & \mathcal{O}(p^{-1}) \\ \mathcal{O}(p) & \mathcal{O}(1) & \mathcal{O}(1) & \mathcal{O}(1) & \mathcal{O}(1) & \mathcal{O}(p^{-1}) \\ \mathcal{O}(p) & \mathcal{O}(1) & \mathcal{O}(1) & \mathcal{O}(1) & \mathcal{O}(1) & \mathcal{O}(p^{-1}) \\ \mathcal{O}(p^2) & \mathcal{O}(p) & \mathcal{O}(p) & \mathcal{O}(p) & \mathcal{O}(p) & \mathcal{O}(1) \end{pmatrix}. \tag{A6}$$

For a homogeneous fluid layer, the usual expressions according to reference [21, (35)] for the elements of $\mathbf{P}_F(\omega, p)$ get the correct magnitude as prescribed by equation (A4) as ω tends to zero with $p = q/\omega$. The expressions according to reference [22, (4)] for the elements of $\mathbf{P}_S(\omega, p)$ for a homogeneous solid layer, on the other hand, contain terms which are at least a factor p, in general a factor p^2, too large as compared to equation (A5). In the same way, most expressions according to

reference [21, (13)] for the elements of the corresponding matrix $\mathbf{B}(\omega, p) = \mathbf{P}_S(\omega, p)^{\Delta_2}$ contain terms which are too large by factors p^2 or p^4 as compared to equation (A6). Numerical precision is lost when these large terms are not cancelled exactly in low-frequency dispersion computations.

However, as is easily verified, the terms of the alternative expressions for the elements of $\mathbf{P}_S(\omega, p)$ and $\mathbf{B}(\omega, p)$ according to reference [21, (38) and (31)–(34)] do indeed exhibit the correct magnitudes as prescribed by equations (A5) and (A6). Hence, they resolve the cancellation problems not only for the slow modes considered in reference [21] but also for the low-frequency modes with $\omega p \approx q \neq 0$.